

Dust shells around carbon Mira variables

M. A. T. Groenewegen,¹* P. A. Whitelock,² C. H. Smith³ and F. Kerschbaum⁴

¹Max-Planck-Institut für Astrophysik, Karl-Schwarzschild-Straße 1, D-85740 Garching, Germany

²South African Astronomical Observatory, PO Box 9, 7935 Observatory, South Africa

³Department of Physics, University College, ADFA, Canberra ACT 2600, Australia

⁴Institut für Astronomie der Universität Wien, Türkenschanzstraße 17, A-1180 Wien, Austria

Accepted 1997 August 28. Received 1997 July 3; in original form 1997 February 5

ABSTRACT

The spectral energy distributions and mid-infrared spectra of 44 carbon Mira variables are fitted using a dust radiative transfer model. The pulsation periods of these stars cover the entire range observed for carbon Miras. The luminosities are derived from a period–luminosity relation. Parameters derived are the distance, the temperature of the dust at the inner radius, the dust mass-loss rate and the ratio of silicon carbide to amorphous carbon dust. The total mass-loss rate is derived from a modified relation between the photon momentum transfer rate (L/c) and the momentum transfer rate of the wind ($\dot{M}v_\infty$). Mass-loss rates between 1×10^{-8} and $4 \times 10^{-5} M_\odot \text{ yr}^{-1}$ are found. We find good correlations between mass-loss rate and pulsation period ($\log \dot{M} = 4.08 \log P - 16.54$), and between mass-loss rate and luminosity ($\log \dot{M} = 3.94 \log L - 20.79$). These relations are not independent, as we assumed a P – L relation. If we had assumed a constant luminosity for all stars, there still would be a significant relation between \dot{M} and P . The dust-to-gas ratio appears to be almost constant up to periods of about 500 d, corresponding to about $7900 L_\odot$, and then to increase by a factor of 5 towards longer periods and higher luminosities. A comparison is made with radiation-hydrodynamical calculations including dust formation. The mass-loss rates predicted by these models are consistent with those derived in this paper. The main discrepancy is in the predicted expansion velocities for models with luminosities below $\sim 5000 L_\odot$. The radiation-hydrodynamical calculations predict expansion velocities which are significantly too large. This is related to the fact that these models need to be calculated with a large C/O ratio to get an outflow in the first place. Such a large C/O ratio is contrary to observational evidence. It indicates that a principal physical ingredient in these radiation-hydrodynamical calculations is still missing. Possibly the winds are ‘clumpy’, which may lead to dust formation on a local scale, or there is an additional outwards directed force, possibly radiation pressure on molecules.

Key words: stars: AGB and post-AGB – stars: carbon – circumstellar matter – stars: mass-loss – stars: variables: other – infrared: stars.

1 INTRODUCTION

One of the main characteristics of asymptotic giant branch (AGB) stars is their large mass-loss rate. Dust grains form in the cool expanding circumstellar envelope, absorb optical radiation and re-emit it in the infrared. Most previous

studies of dust shells around AGB stars concentrated on oxygen-rich Miras and OH/IR stars (e.g. Rowan-Robinson & Harris 1983a; Bedijn 1987; Schutte & Tielens 1989; Justanont & Tielens 1992; Griffin 1993; Le Sidaner & Le Bertre 1993) or on the well-known carbon star IRC + 10216 (e.g. Mitchell & Robinson 1980; Le Bertre 1987; Martin & Rogers 1987; Griffin 1990; Orofino et al. 1990; Danchi et al. 1994; Winters et al. 1994; Bagnulo, Doyle & Griffin 1995; Ivezić & Elitzur 1996; Groenewegen 1997a).

*E-mail: groen@mpa-garching.mpg.de

Rowan-Robinson & Harris (1983b) considered a sample of 44 carbon stars, but no *IRAS* and Low Resolution Spectrograph (LRS) data were available at the time. Rowan-Robinson et al. (1986) fitted the spectral energy distributions (SEDs) of five carbon stars, fixing the dust temperature at the inner radius at 1000 K. They also assumed a dust absorption law of $\sim \lambda^{-1}$ for all wavelengths, without considering the presence of silicon carbide (SiC), which has a feature near 11.3 μm . Le Bertre (1988b) fitted three carbon stars. Chan & Kwok (1990) fitted SEDs of 145 carbon stars with an LRS classification of 4n (indicating SiC emission), and they therefore missed some carbon stars with weak SiC emission (which sometimes have an LRS=1n classification) and extreme carbon stars which have an LRS=2n classification. They fixed the dust temperature at the inner radius at 1500 K and included only SiC dust in their model. Lorenz-Martins & Lefèvre (1993, 1994) fitted nine and 32 carbon stars, respectively. In their 1993 paper they used the same inner radius for both SiC and amorphous carbon (AMC) grains. In their 1994 paper they allowed for different inner radii for the two dust species. In a recent paper Lorenz-Martins (1996) fitted eight J-type carbon stars.

In Groenewegen (1995a, hereafter G95) the SEDs and LRS spectra of 21 carbon stars were fitted, concentrating on ‘infrared’ carbon stars, i.e., those with thick dust shells. Different types of SiC were tested, and it was concluded that in 18 of 21 cases α -SiC fitted the observed feature. The inner radii for SiC and for AMC were taken to be identical. In agreement with the results of Lorenz-Martins & Lefèvre (1993, 1994), it was found that the radio SiC/AMC decreases with increasing optical depth of the shell.

In the present paper we concentrate on carbon-rich Mira variables (from now on we mean carbon-rich Miras by the term Miras unless otherwise noted). The main advantage of using Miras is that the period–luminosity relation provides reasonably accurate distances for such stars, largely eliminating the uncertainty of some of the fitted parameters on distance. Secondly, using Miras enables a study to be made of the relation between mass-loss rate and pulsation period, or mass-loss rate and luminosity, which is important from an evolutionary point of view. To this end we took the 10 stars from G95 with measured pulsation periods, and selected 34 other stars from the literature to cover the entire known range of periods for Miras.

As preliminary results indicated that the mass-loss rate of Miras with periods below 400 d may be lower than that expected from an extrapolation of the results for longer periods (Groenewegen 1995b,c), emphasis was put on the selection of short-period Miras.

The paper is organized as follows. In Section 2 the radiative transfer model is introduced. In Section 3 the period–luminosity relation is presented. In Section 4 new observations are discussed. In Section 5 the fits to the SEDs and LRS spectra are presented. In Section 6 the final values of the mass-loss rate and dust-to-gas ratio are derived, and the results are discussed in Section 7.

2 THE MODEL

The radiative transfer model of Groenewegen (1993) is used. This model was developed to handle non- r^2 density

distributions in spherically symmetric dust shells. It simultaneously solves the radiative transfer equation and the thermal balance equation for the dust.

When the input spectrum of the central source is fixed, the shape of the SED is exclusively determined by the dust optical depth, defined by

$$\begin{aligned} \tau_\lambda &= \int_{r_{\text{inner}}}^{r_{\text{outer}}} \pi a^2 Q_\lambda n_d(r) dr \\ &= 5.405 \times 10^8 \frac{\dot{M} \Psi Q_\lambda / a}{R_* v_\infty \rho_d r_c} \int_1^{x_{\text{max}}} \frac{R(x)}{x^2 w(x)} dx, \end{aligned} \quad (1)$$

where $x = r/r_c$, $\dot{M}(r) = \dot{M}R(x)$, and $v(r) = v_\infty w(x)$. The normalized mass-loss rate profile $R(x)$ and the normalized velocity law $w(x)$ should obey $R(1) = 1$ and $w(\infty) = 1$, respectively. In the case of a constant mass-loss rate and a constant velocity, the integral in equation (1) is essentially unity, since x_{max} is always much larger than 1. The symbols and units in equation (1) are: the (present-day) mass-loss rate \dot{M} in $M_\odot \text{yr}^{-1}$, Ψ the dust-to-gas mass ratio (assumed constant with radius), Q_λ the extinction coefficient, a the grain size in cm (the model assumes a single grain size), R_* the stellar radius in R_\odot , v_∞ the terminal velocity of the dust in km s^{-1} , ρ_d the dust grain specific density in g cm^{-3} , r_c the inner dust radius in units of stellar radii, and x_{max} the outer radius in units of r_c . It should be noted that from the model fitting only the dust mass-loss rate can be determined, i.e., $\dot{M} \times \Psi$.

In a detailed study of IRC + 10216 (Groenewegen 1997a) it was found that including a velocity law to calculate the density, i.e., $1/[r^2 v(r)]$, gave somewhat worse results than using a simple r^{-1} law. It was argued that since the dust-to-gas ratio is also an increasing function of radius, the two effects tend to cancel. Fully consistent models (Winters 1994) lend some support to this idea. A constant velocity is therefore assumed as well as a constant mass-loss rate. On the other hand, if some specific velocity law were adopted, then this would simply lead to a rescaling of the mass-loss rate in such a way as to obtain the same optical depth as with a constant velocity.

Unless otherwise specified, the outer radius is determined in the model by a dust temperature of 20 K, and a grain specific density of $\rho_d = 2.0 \text{ g cm}^{-3}$ is adopted.

In most models the terminal velocity of the dust is assumed to be equal to that of the gas. This, however, neglects the drift velocity of the dust with respect to the gas ($v_{\text{dust}} = v_{\text{gas}} + v_{\text{drift}}$), which may be estimated from (e.g. Kwan & Hill 1977)

$$v_{\text{drift}} = 1.43 \times 10^{-4} \times \left[\frac{L Q_F(r) v_\infty^{\text{gas}}}{\dot{M}} \right]^{0.5} \text{ km s}^{-1}, \quad (2)$$

where v_∞^{gas} is the terminal velocity of the gas; L is the stellar luminosity in solar units, and $Q_F(r)$ is the flux-weighted extinction coefficient, defined as $Q_F(r) = \int F_\lambda(r) Q_\lambda d\lambda / \int F_\lambda(r) d\lambda$. In Section 6 the influence of the drift velocity on the mass-loss rates is discussed.

The central star is represented by a blackbody, modified to allow for the characteristic absorption feature in carbon stars at 3.1 μm due to HCN and C_2H_2 (e.g. Ridgway, Carbon & Hall 1978):

$$B_{\lambda}(T_{\text{eff}}) \exp \left\{ -A \exp \left[-\left(\frac{\lambda - \lambda_0}{\Delta\lambda} \right)^2 \right] \right\}, \quad (3)$$

with $\lambda_0 = 3.1 \mu\text{m}$. This novelty is introduced to enable a direct fit to the observed 2–4 μm spectra of some stars. Following Groenewegen, de Jong & Geballe (1994), values of $A = 4.605$ and $\Delta\lambda = 0.075 \mu\text{m}$ are adopted. The value of A provides a flux in the 3.1- μm feature which is 1 per cent of the continuum in a star without a circumstellar shell.

For the dust composition a combination of AMC and SiC grains is assumed. For simplicity, a single condensation temperature is used. In principle, SiC and AMC could have different temperature profiles, but to take this into account requires two additional free parameters (a second condensation temperature and dust-to-gas ratio). Since the abundance of SiC is found to be small, the simplification of the temperature profile seems to be justified. In equation (1) the value of Q_{λ}/a is calculated from $Q_{\lambda}/a = x(Q_{\lambda}/a)^{\text{SiC}} + (1-x)(Q_{\lambda}/a)^{\text{AMC}}$, where $x \in [0, 1]$ is determined by the fit to the LRS spectrum. The absorption coefficient for AMC is calculated from the optical constants listed in Rouleau & Martin (1991) for their AC1-species.

It was shown in G95 that most of the SiC features can be fitted with α -SiC (Pégourié 1988). The optical constants from that paper are therefore adopted.

Beam effects are taken into account. This is especially important for longer wavelengths ($\lambda \gtrsim 50 \mu\text{m}$), where the emission becomes extended relative to the typical beams used in far-infrared observations. In particular, for $\lambda < 7 \mu\text{m}$ a Gaussian beam with a full-width at half-maximum (FWHM) of 20 arcsec is assumed (typical of near-infrared observations). In the range $7 < \lambda < 140 \mu\text{m}$ the beam effects of the *IRAS* detectors are taken into account (for details see Groenewegen 1993). For $\lambda > 140 \mu\text{m}$ a Gaussian beam of FWHM = 18.5 arcsec is assumed, representative of the far-infrared observations to which the model is compared.

In the models the calculated energy distribution is convolved with the spectral response of the *IRAS* filters (Table II.C.5 of the Explanatory Supplement) to compare the predicted flux densities directly to the flux densities listed in the *IRAS* Point Source or Faint Source Catalogs.

3 PERIOD–LUMINOSITY RELATION

To estimate the luminosity from the pulsation periods we use the period–luminosity (P – L) relation from Groenewegen & Whitelock (1996):

$$M_{\text{bol}} = -2.59 \log P + 2.02. \quad (4)$$

This relation was derived for carbon Miras in the Large Magellanic Cloud, and was shifted by the distance modulus of 18.5 mag to obtain the P – L relation for carbon Miras in our Galaxy. The relation was derived for periods below 520 d, but new data for likely carbon-rich Miras with periods up to 900 d in the LMC appear to lie on an extrapolation (Groenewegen et al. 1997). Equation (4) is therefore used for all periods to obtain the luminosity (Table 2, column 5).

The derived distances and dust mass-loss rates (see Table 2) depend on the assumed luminosity, so that $D \propto \sqrt{L}$, and $\dot{M} \propto \sqrt{L}$.

4 OBSERVATIONS

The models are fitted to the observed SEDs and mid-infrared spectra. Most of the data come from the literature (see column 10 in Table 2). However, some new or previously unpublished data are also used as constraints, in particular for some of the stars with few published photometric, or poor mid-infrared spectroscopic data.

Mid-infrared spectra of R CMi, TV Vel, V Cru, VX Gem, ZZ Gem and R Ori were taken on 1994 November 25–27 with the UCL infrared cooled grating array spectrometer (for details see Aitken & Roche 1982) mounted at the $f/36$ Cassegrain focus of the 3.9-m Anglo-Australian Telescope (AAT). We used a circular aperture of 4.2-arcsec diameter, while the (optical) seeing was in the range 1.0–1.5 arcsec for most of the time. The 8.0 to 13.0 μm window was covered with 25 detectors, resulting in an effective resolution of $\lambda/\Delta\lambda \approx 50$. The grating was stepped once, offset by one and a half detector widths, providing an oversampled (50 data point) spectrum, which was subsequently smoothed. Chopping, with a frequency of 12.5 Hz, and beam-switching were employed, each using a throw of 15 arcsec in declination. The pointing of the telescope was regularly verified on a bright nearby star. The observations were obtained through cirrus clouds, and this is reflected by the large error bars. Flux calibration and correction for telluric absorption were made by reference to the F0 II star α Car.

Mid-infrared spectra were obtained of RT Gem on 1995 January 12, of V Aur and R CMi on 1995 January 14, and of CN Per and UV Aur on 1995 August 21, respectively. The common-user instrument CGS3 was used at the 3.8-m UKIRT telescope under photometric conditions during service observing. The spectra were wavelength-calibrated using a Kr lamp; the accuracy of the fit is 0.01 μm rms. Flux calibration and correction for telluric absorption were made by reference to BS 1708 (for UV Aur, V Aur and CN Per) and BS 2990 (for RT Gem and R CMi).

Table 1 lists *JHKL* magnitudes for six of the stars under discussion, obtained on the 0.75-, 1.0- or 1.9-m telescopes at SAAO as specified in the table. The photometry is on the SAAO system as defined by Carter (1990). It is accurate to better than ± 0.03 mag at *JHK* and better than ± 0.05 mag at *L*. Note that a small number of the older measurements of R CMi and TV Vel were reported by Catchpole et al. (1979). The measurements listed here differ slightly from those in the earlier paper as they have been corrected to Carter’s improved values for the standard stars.

CN Per was observed on 1996 August 8 with the 1.5-m Carlos Sanchez telescope at the Teide Observatory on the island of Tenerife, with the following result: $J = 7.02$, $H = 5.81$, $K = 4.98$.

5 THE FITTING PROCEDURE

In Table 2 some general parameters of the stars are listed. The sample is a selection of Miras, ranging from stars with low-to-moderate mass-loss rates to the reddest carbon stars known. The stars have been selected for the availability of as many flux determinations over as large a wavelength region as possible, and cover the whole range of known Mira periods.

Table 1. SAAO near-infrared photometry.

| JD-2440000 | <i>J</i> | <i>H</i> | <i>K</i> | <i>L</i> | Tel. |
|------------|----------|----------|----------|----------|------|
| ZZ Gem | | | | | |
| 8586.52 | 5.08 | 3.71 | 3.03 | 2.46 | 0.75 |
| 8629.39 | 5.58 | 4.10 | 3.26 | 2.61 | 0.75 |
| 8668.32 | 5.80 | 4.34 | 3.39 | 2.72 | 0.75 |
| 8965.50 | 5.54 | 4.03 | 3.20 | 2.48 | 0.75 |
| 8986.43 | 5.58 | 4.10 | 3.26 | 2.59 | 0.75 |
| 9061.25 | 5.08 | 3.86 | 3.22 | 2.69 | 0.75 |
| 9382.37 | 5.02 | 3.79 | 3.16 | 2.64 | 0.75 |
| 9639.63 | 5.56 | 4.14 | 3.30 | 2.73 | 0.75 |
| 9672.55 | 5.31 | 4.01 | 3.26 | 2.74 | 0.75 |
| RT Gem | | | | | |
| 8586.56 | 6.15 | 4.86 | 4.33 | 3.85 | 0.75 |
| 8633.39 | 6.58 | 5.26 | 4.61 | 4.22 | 0.75 |
| 8669.33 | 6.90 | 5.58 | 4.87 | 4.53 | 0.75 |
| 8965.53 | 6.31 | 5.02 | 4.47 | 4.02 | 0.75 |
| 8986.47 | 6.49 | 5.18 | 4.60 | 4.21 | 0.75 |
| 9061.29 | 6.65 | 5.48 | 4.90 | 4.54 | 0.75 |
| 9376.35 | 6.80 | 5.56 | 4.89 | 4.57 | 1.9 |
| 9639.65 | 6.13 | 4.84 | 4.36 | 3.96 | 0.75 |
| 9672.57 | 6.36 | 5.09 | 4.52 | 4.13 | 0.75 |
| R CMi | | | | | |
| 2036.50 | 3.58 | 2.62 | 2.24 | 1.90 | 1.0 |
| 5007.39 | 4.13 | 3.15 | 2.78 | 2.36 | 0.75 |
| 5688.48 | 4.09 | 3.14 | 2.75 | 2.43 | 0.75 |
| 8589.55 | 4.58 | 3.48 | 2.92 | 2.71 | 0.75 |
| 8632.46 | 4.40 | 3.35 | 2.91 | 2.61 | 0.75 |
| 8669.35 | 4.24 | 3.22 | 2.84 | 2.51 | 0.75 |
| 8962.53 | 4.32 | 3.24 | 2.83 | 2.43 | 0.75 |
| 8987.47 | 4.26 | 3.21 | 2.81 | 2.37 | 0.75 |
| 9056.30 | 3.67 | 2.60 | 2.25 | 1.78 | 0.75 |
| 9376.34 | 3.93 | 2.90 | 2.51 | 2.16 | 1.9 |
| 9642.63 | 4.34 | 3.30 | 2.87 | 2.43 | 0.75 |
| 9672.58 | 4.14 | 3.13 | 2.77 | 2.34 | 0.75 |
| VX Gem | | | | | |
| 8589.56 | 5.14 | 3.82 | 3.10 | 2.68 | 0.75 |
| 8633.40 | 5.47 | 4.16 | 3.33 | 2.97 | 0.75 |
| 8669.34 | 5.61 | 4.34 | 3.49 | 3.18 | 0.75 |
| 8962.54 | 4.96 | 3.65 | 3.00 | 2.62 | 0.75 |
| 8986.50 | 5.15 | 3.82 | 3.11 | 2.74 | 0.75 |
| 9058.27 | 5.43 | 4.17 | 3.38 | 3.06 | 0.75 |
| 9376.36 | 5.19 | 3.86 | 3.14 | 2.74 | 1.9 |
| 9641.65 | 4.37 | 3.22 | 2.82 | 2.47 | 0.75 |
| 9673.58 | 4.46 | 3.25 | 2.81 | 2.37 | 0.75 |
| TV Vel | | | | | |
| 2035.50 | 5.23 | 3.99 | 3.18 | 2.96 | 0.75 |
| 2552.50 | 5.03 | 3.90 | 3.26 | 2.97 | 0.75 |
| 3515.55 | 5.02 | 3.87 | 3.38 | 2.80 | 0.75 |
| 4336.40 | 4.98 | 3.84 | 3.30 | 2.79 | 0.75 |
| 8665.56 | 5.16 | 3.97 | 3.38 | 2.86 | 0.75 |
| 8735.37 | 5.11 | 3.90 | 3.42 | 2.87 | 0.75 |
| 8967.57 | 5.26 | 3.88 | 3.14 | 2.73 | 0.75 |
| 9001.44 | 5.47 | 4.12 | 3.31 | 2.86 | 0.75 |
| 9061.44 | 5.39 | 4.13 | 3.42 | 3.01 | 0.75 |
| 9107.33 | 5.11 | 3.93 | 3.38 | 2.85 | 0.75 |
| 9173.22 | 5.10 | 3.91 | 3.43 | 2.86 | 0.75 |
| 9379.57 | 5.22 | 3.87 | 3.12 | 2.62 | 0.75 |
| 9403.48 | 5.37 | 4.00 | 3.23 | 2.83 | 0.75 |
| 9677.57 | 4.68 | 3.46 | 3.02 | 2.50 | 0.75 |
| R Cap | | | | | |
| 2551.50 | 5.79 | 4.33 | 3.30 | 2.06 | 0.75 |
| 2593.50 | 6.30 | 4.64 | 3.54 | 2.37 | 0.75 |
| 8786.60 | 5.52 | 3.98 | 3.02 | 1.98 | 0.75 |
| 8876.37 | 6.17 | 4.64 | 3.52 | 2.64 | 0.75 |
| 9146.56 | 5.46 | 3.96 | 3.05 | 2.13 | 0.75 |
| 9213.48 | 5.91 | 4.40 | 3.38 | 2.55 | 0.75 |
| 9231.37 | 5.83 | 4.37 | 3.38 | 2.56 | 0.75 |
| 9639.33 | 5.87 | 4.21 | 3.28 | 2.40 | 0.75 |
| 9673.25 | 5.09 | 3.85 | 3.04 | 2.10 | 0.75 |

Table 2 lists the *IRAS* and GCVS names, the pulsation period, the full amplitude in the *K* band when available, the luminosity derived from equation (4), the galactic coordinates, the interstellar extinction in the *V* band (see below), the terminal gas velocity of the envelope, and the references to the photometry used to construct the SEDs. LRS spectra are either taken from the LRS atlas (1986), or from the data base available at the University of Calgary. The LRS spectra are corrected according to Cohen, Walker & Witteborn (1992). No LRS spectra are available for Y Per, R Ori and RT Gem. Y Per is nevertheless included, as it is the carbon Mira with the shortest pulsation period. For RT Gem a UKIRT 7–13 μm spectrum is available, and for R Ori an AAT spectrum.

The interstellar extinction at *V* was estimated, either from Neckel & Klare (1980) (who list observed values of A_V as a function of galactic coordinates and distance) for stars with $|b| \lesssim 7^\circ$, or from Burnstein & Heiles (1982) for those with $|b| \gtrsim 10^\circ$. Parenago's (1940) model was used for those stars outside of the range covered by these two papers, and to obtain a second estimate for those in range (see Groenewegen et al. 1992 for the exact form). The estimates of A_V usually agree, and the adopted values are listed in Table 2.

The fitting procedure is as follows. Typically, four values for the dust temperature at the inner radius (T_{inn}) are chosen. The mass-loss rate (assumed constant) is varied to fit the (shape of the) SED and mid-infrared spectra. The distance is determined by demanding that the predicted and observed mean near-infrared magnitudes agree. The SiC feature is fitted by changing the (mass) ratio SiC/AMC. This last step is straightforward, since the strength of the SiC feature turns out to scale linearly with the adopted SiC/AMC ratio. In choosing the best value for T_{inn} , equal weight is given to the fits of the SED and the LRS spectrum. If necessary, the aforementioned steps are repeated for the final choice of T_{inn} . For most stars the default value of 2500 K for the effective temperature of the central star gives good results. For some stars a different value gives better results. The formal errors in the mass-loss rate and T_{inn} are estimated to be 20 per cent (3σ).

For two stars interferometric visibility curves are fitted as well. IRC + 10216 is discussed in detail in Groenewegen (1997a). A best-fitting grain size of 0.16 μm was derived. For IRAS 15194 – 51125 the *K*- and *L*-band visibility curves as presented by Lopez et al. (1993) were fitted. A best-fitting grain size of 0.10 μm is derived.

The best-fitting models are shown in Figs 1–43, except that of CW Leo which is extensively discussed in Groenewegen (1997a). The spectra have been corrected for interstellar extinction using A_V from Table 2 and the interstellar extinction curve of Cardelli, Clayton & Mathis (1989). The corresponding model parameters are included in Table 3, which lists the *IRAS* name, the temperature of the dust at the inner radius, the effective temperature of the central stars, the dust mass-loss rate (assuming the standard values for the dust opacity dust-to-gas ratio, and furthermore assuming that the dust velocity equals the gas velocity, thereby neglecting the drift velocity; see Section 6), the inner dust radius, the ratio of SiC to AMC, the derived distance for the assumed luminosity from Table 2, the optical depth at 11.33 and 0.5 μm , the flux-weighted optical

Table 2. The programme stars.

| IRAS-name | GCVS | Period ^(a) (days) | ΔK ^(b) (mag) | Lum. (L_{\odot}) | l | b | A_V (mag) | v_{∞} ^(c) (kms^{-1}) | photometry ^(d) |
|------------|-----------|---------------------------------|------------------------------------|-------------------------|-------|-------|----------------|--|--------------------------------|
| 01144+6658 | – | 1060 (5) | 2.4 | 16380 | 125.5 | 4.5 | 2.5 | 18.1 (2) | 16, 29, 39, 48, 53 |
| 02032+5636 | CN Per | 384 (1) | – | 5720 | 133.1 | –44.5 | 1.8 | (10:) (6) | 61 |
| 02270–2619 | R For | 388.7 (1) | 0.84 | 5790 | 215.8 | –68.1 | 0.1 | 16.9 (3) | 6,20,30,36,37,53,54,58 |
| 02293+5749 | – | 815 (5) | 2.5 | 12470 | 136.1 | –2.2 | 3.0 | 14.2 (1) | 16, 20, 29, 53 |
| 03229+4721 | V384 Per | 535 (1) | 1.4 | 8060 | 148.2 | –7.6 | 1.1 | 15.5 (2) | 4, 10, 22, 30, 41 |
| 03243+4400 | Y Per | 252.3 (4) | – | 3700 | 150.3 | –10.2 | 1.0 | 7.2 (3) | 3, 5, 30, 49 |
| 03488+3943 | V414 Per | 515 (2) | 1.0 | 7750 | 156.6 | –10.9 | 1.1 | 30.7 (2) | 27, 30, 41, 48, 53 |
| 04562+0803 | R Ori | 378.0 (4) | 0.7 | 5630 | 191.7 | –20.5 | 0.4 | 10(:) (3) | 3, 6, 30, 58 |
| 04573–1452 | R Lep | 427.1 (1) | 0.6 | 6380 | 214.3 | –31.3 | 0.2 | 19.0 (1) | 7,18,26,30,32,33,37,50,53,58 |
| 05185+3227 | UV Aur | 394.4 (1) | 0.67 | 5880 | 174.2 | –2.4 | 1.0 | (10:) (6) | 30, 46, 50, 51, 53, 60 |
| 06012+0328 | V1259 Ori | 696 (3) | 1.73 | 10590 | 200.8 | –7.0 | 1.3 | 16.5 (2) | 22, 27, 37 |
| 06202+4743 | V Aur | 353 (1) | – | 5240 | 166.8 | 15.4 | 0.7 | 20(:) (3) | 3, 4, 30 |
| 06209+2503 | ZZ Gem | 317.0 (1) | 0.33 | 4690 | 187.6 | 5.5 | 1.6 | 6.8 (3) | 5, 10, 30, 47, 50, 61 |
| 06230–0930 | – | 494 (3) | 1.40 | 7430 | 218.6 | –10.1 | 1.5 | 16.6 (3) | 8, 20, 21, 37, 53 |
| 06342+0328 | V688 Mon | 653 (3) | 1.48 | 9910 | 208.2 | –1.7 | 2.7 | 13.3 (1,3) | 20, 21, 22, 25, 37 |
| 06436+1840 | RT Gem | 350.4 (1) | 0.57 | 5200 | 195.7 | 7.3 | 1.0 | (10:) (6) | 61 |
| 06529+0626 | CL Mon | 497.2 (1) | 0.7 | 7470 | 207.7 | 3.8 | 0.8 | 26.1 (1,3) | 13, 30, 50, 53, 58 |
| 07059+1006 | R CMi | 337.8 (1) | 0.68 | 5010 | 205.9 | 8.4 | 0.8 | (10:) (6) | 3,6,18,26,30,40,50,53,58,61 |
| 07065–7256 | R Vol | 453.6 (1) | 0.9 | 6800 | 284.2 | –24.8 | 0.5 | 20.3 (1,3) | 6, 13, 15, 30, 53, 58 |
| 07098–2012 | – | 725 (3) | 1.30 | 11050 | 233.3 | –4.8 | 1.0 | 24.0 (1,2) | 21, 22, 37 |
| 07099+1441 | VX Gem | 379.4 (1) | 0.68 | 5650 | 202.2 | 11.3 | 0.6 | (10:) (6) | 30, 50, 53, 61 |
| 08434–2801 | R Pyx | 364.7 (1) | – | 5420 | 251.3 | 9.2 | 0.9 | 8.8 (3) | 6, 13, 30, 58 |
| 09452+1330 | CW Leo | 630 (2,3) | 2.03 | 9550 | 221.5 | 45.1 | 0.1 | 14.5 (1,2) | 24 |
| 10324–5358 | TV Vel | 365.2 (1) | 0.40 | 5430 | 283.7 | 3.4 | 1.0 | (10:) (6) | 61 |
| 12447+0425 | RU Vir | 433.2 (1) | 1.0 | 6480 | 300.3 | 67.0 | 0.1 | 15.4 (2) | 6,11,15,17,19,30,45,50,53 |
| 12536–5737 | V Cru | 376.5 (1) | 0.4 | 5600 | 303.6 | 5.0 | 1.4 | (10:) (6) | 6, 30, 58, 59 |
| 15194–5115 | – | 580 (3) | 1.16 | 8770 | 325.5 | 4.7 | 0.8 | 22.2 (4) | 12, 22, 37, 44, 52 |
| 15477+3943 | V CrB | 357.6 (1) | – | 5310 | 63.3 | 51.2 | 0.1 | 8.1 (3) | 2, 4, 14, 18, 26, 30, 53, 55 |
| 16239–1218 | V Oph | 297.2 (1) | 0.54 | 4390 | 3.0 | 24.5 | 0.6 | 7.0 (3) | 18, 20, 28, 30, 31, 34, 50, 53 |
| 17556+5813 | T Dra | 421.6 (1) | – | 6300 | 86.8 | 29.9 | 0.1 | 13.1 (1) | 14, 17, 18, 26, 50, 53 |
| 19008+0726 | – | 577 (3) | 1.32 | 8720 | 41.0 | 0.8 | 1.6 | 26.0 (3) | 37, 47, 50, 53 |
| 19175–0807 | – | 676 (3) | 1.41 | 10280 | 29.0 | –10.1 | 0.9 | 27.5 (3) | 8, 22, 27, 37, 53 |
| 19321+2757 | V1965 Cyg | 625 (2) | 1.9 | 9470 | 62.6 | 4.0 | 1.5 | 26.0 (1,2) | 20, 22, 27, 50 |
| 19594+4047 | V1968 Cyg | 783 (2) | 1.6 | 11970 | 76.5 | 5.6 | 1.2 | 21.5 (2) | 1, 22, 23, 27, 43 |
| 20072+3116 | V1969 Cyg | 550 (2) | 1.9 | 8300 | 69.4 | –0.9 | 2.3 | 25.6 (2) | 8, 22, 27, 43, 53 |
| 20085–1425 | R Cap | 345.2 (1) | 0.54 | 5120 | 28.6 | –24.0 | 0.3 | 10.5 (3) | 8, 25, 30, 61 |
| 20396+4757 | V Cyg | 421 (1) | – | 6290 | 86.5 | 3.8 | 0.9 | 13.2 (1) | 2, 4, 20, 22, 30, 35 |
| 20570+2714 | – | 750 (2) | 1.6 | 11440 | 72.6 | –12.0 | 0.8 | 25.8 (3) | 8, 9, 19, 27, 53 |
| 21035+5136 | V1549 Cyg | 533 (2) | 1.4 | 8030 | 91.8 | 3.2 | 1.2 | 11.4 (1) | 8, 10, 27, 42, 50, 53, 56 |
| 21262+7000 | AX Cep | 395 (1) | – | 5890 | 107.2 | 13.9 | 1.2 | 13.2 (2) | 30, 47, 53 |
| 21320+3850 | V1426 Cyg | 470 (1) | ~0.8 | 7050 | 86.3 | –9.4 | 0.9 | 13.9 (1,2) | 10, 20, 26, 30, 50, 53 |
| 22036+3315 | RZ Peg | 438.7 (1) | – | 6570 | 87.6 | –17.8 | 0.5 | 12.6 (5) | 3, 30, 32, 50, 51 |
| 23166+1655 | – | 696 (3) | 1.90 | 10590 | 93.5 | –40.4 | 0.1 | 14.6 (1,2) | 22, 23, 27, 37, 38, 52, 57 |
| 23320+4316 | LP And | 620 (2) | 2.1 | 9400 | 108.5 | –17.1 | 0.5 | 14.7 (1,2) | 8, 20, 22, 27, 30, 41 |

(a) Between parentheses the references for the pulsation period: 1=GCVS (Kholopov et al. 1985), 2=Jones et al. (1990), 3=Le Bertre (1992), 4=SIMBAD data base, 5=Joyce et al. 1997, in preparation.

(b) Full amplitude in the K band.

(c) Between parentheses the references for the gas expansion velocity: 1=average of values in Loup et al. (1993), 2=Groenewegen et al. (1996a), 3=Groenewegen et al. (1996b) 4=Nyman et al. (1993b), (5) Sahai & Liechti (1995), (6)=not available, a value of 10 km s^{-1} has been adopted. Uncertain values are indicated by a colon.

(d) References for the photometry used: 1=Alknis (1980), 2=Altenhoff, Thum & Wendker (1994), 3=Barnes (1997), 4=Bergeat et al. (1976), 5=Bergeat & Lunel (1980), 6=Catchpole et al. (1979), 7=Celis (1982), 8=Cohen & Kuhl (1977), 9=Cohen (1984), 10=Dyck, Lockwood & Capps (1974), 11=Engen (1975), 12=Epchtein et al. (1987), 13=Epchtein, Le Bertre & Lépine (1990), 14=Forrest, Gillett & Stein (1975), 15=Fouqué et al. (1992), 16=Gehrz & Hackwell (1976), 17=Gehrz et al. (1984), 18=Gillett, Merrill & Stein (1971), 19=Gosnell, Hudson & Puetter (1979), 20=Grasdalen et al. (1983), 21=Groenewegen & de Jong (1993), 22=Groenewegen, de Jong & Baas (1993), 23=Groenewegen et al. (1994), 24=Groenewegen (1997a), 25=Guglielmo et al. (1993), 26=Hackwell (1972), 27=Jones et al. (1990), 28=Jørgensen & Westerlund (1988), 29=Joyce et al. (1997, in preparation), 30=Kholopov et al. (1985), 31=Landolt (1968), 32=Landolt (1969a), 33=Landolt (1969b), 34=Landolt (1973), 35=Lázano et al. (1994), 36=Le Bertre (1988a), 37=Le Bertre (1992), 38=Lebofsky & Rieke (1977), 39=Lebofsky et al. (1978), 40=Lockwood (1972), 41=Lockwood (1974), 42=Lockwood (1985), 43=Low et al. (1976), 44=Meadows, Good & Wolstencroft (1987), 45=Merrill & Stein (1976), 46=Munari et al. (1992), 47=Neugebauer & Leighton (1969), 48=Ney & Merrill (1980), 49=Nicolet (1978), 50=Noguchi et al. (1981), 51=Olson & Richer (1975), 52=Omont et al. (1996, private communication), 53=Price & Murdock (1983), 54=Richer (1971), 55=Simon (1976), 56=Strecker & Ney (1974), 57=Sopka et al. (1985), 58=Walker (1979), 59=Whitelock et al. (1997), 60=Woolf (1973), 61=this paper. In addition, the IRAS PSC or FSC flux densities and IRS spectra (when available), corrected according to Cohen et al. (1992), or newly obtained mid-IR spectra (see Section 4) are used.

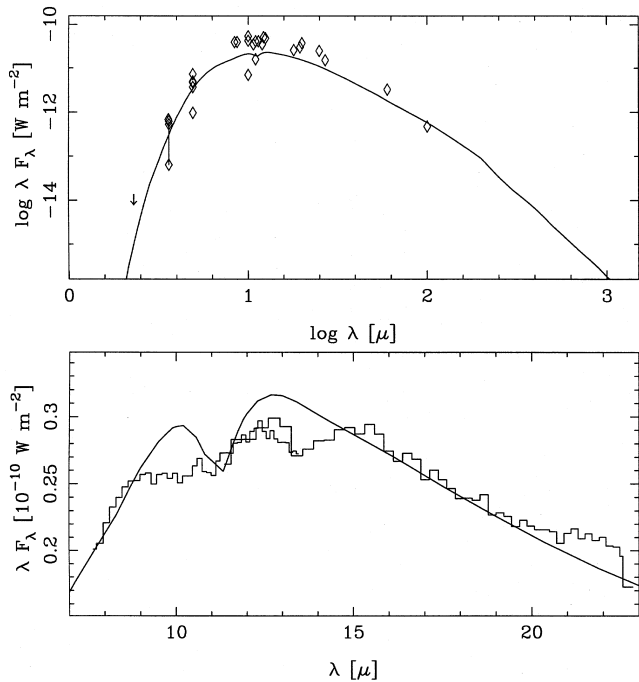


Figure 1. IRAS 01144 + 6658 (AFGL 190). The remaining part of this caption refers to Figs 1–43 in general. The model is represented by the solid line, the observations by the symbols and the histogram, in the case of the LRS spectra. The submillimetre data have error bars. Observations at minimum and maximum light are connected. Upper limits are indicated by a \downarrow . There usually is a kink in the model curve beyond 200 μm , which is due to beam effects.

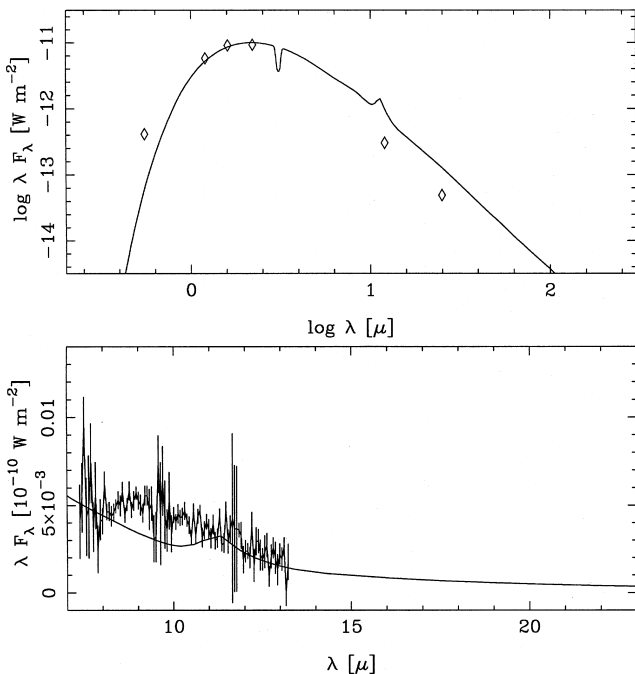


Figure 2. IRAS 02032 + 5636 (CN Per). The 8–13 μm spectrum represents the (unscaled) UKIRT spectrum.

depth (defined as $\tau_F(r) = \int F_\lambda(r) \tau_\lambda d\lambda / \int F_\lambda(r) d\lambda$), the flux-weighted extinction coefficient for a grain size of 0.1 μm , and a remarks column which usually gives the number in the AFGL catalogue, as an alternative for the GCVS name listed in Table 2.

The derived dust mass-loss rates are subject to the following systematic effects. Following equation (1), the mass-loss rate scales like $\sim R_* v_\infty / \kappa_\lambda$, where κ_λ is the dust opacity. For

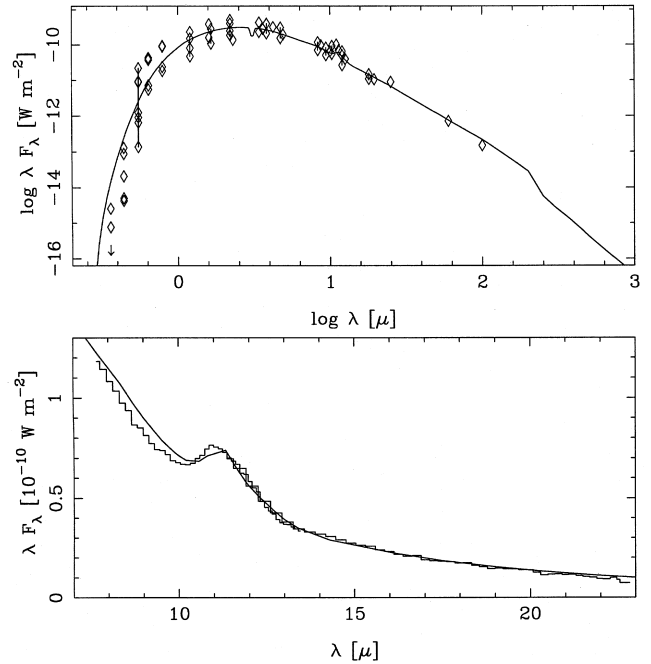


Figure 3. IRAS 02270 – 2619 (R For).

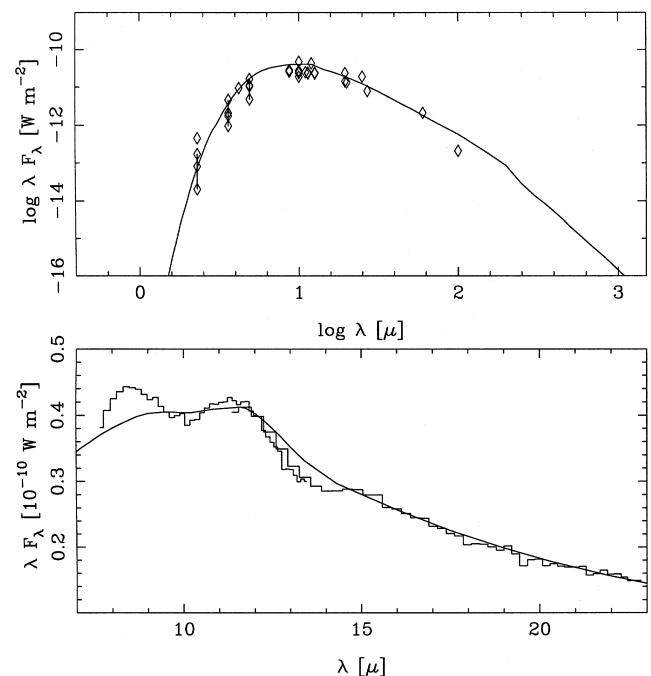


Figure 4. IRAS 02293 + 5749 (AFGL 341).

a constant effective temperature, the derived dust mass-loss rates (and derived distances) scale like \sqrt{L} . The opacity at 60 μm for the adopted absorption coefficient ($\kappa = 3Q/4a\rho_d$) is $68 \text{ cm}^2 \text{ g}^{-1}$. This is about a factor of 2 lower than the usually quoted value of $\sim 160 \text{ cm}^2 \text{ g}^{-1}$ (see, e.g., Jura 1986). Since the mass-loss rate scales like κ^{-1} , the values quoted in Table 3 may be systematically too high by about a factor of 2.

The fits to the SEDs and mid-IR spectra are generally of good quality. Problems can arise when there is little obser-

vational data (e.g., CN Per; Fig. 2). The bad fits may in some cases also be due to the simple blackbody approximation for the emission from the central star, in particular when the mass-loss rate is small and the photospheric contribution to the total flux becomes important.

As found in G95, the α -SiC opacity provides good fits to the observed features in most cases. When it does not, the observed feature peaks at shorter wavelengths [e.g., AFGL

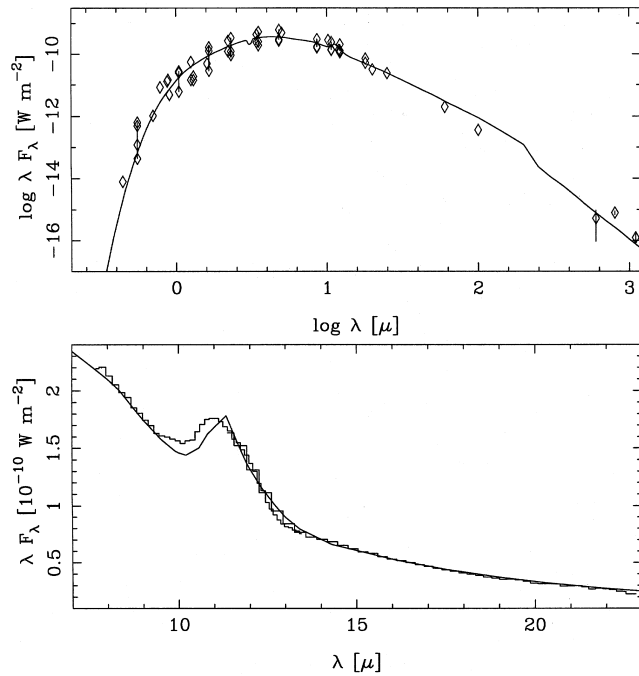


Figure 5. IRAS 03229 + 4721 (AFGL 489).

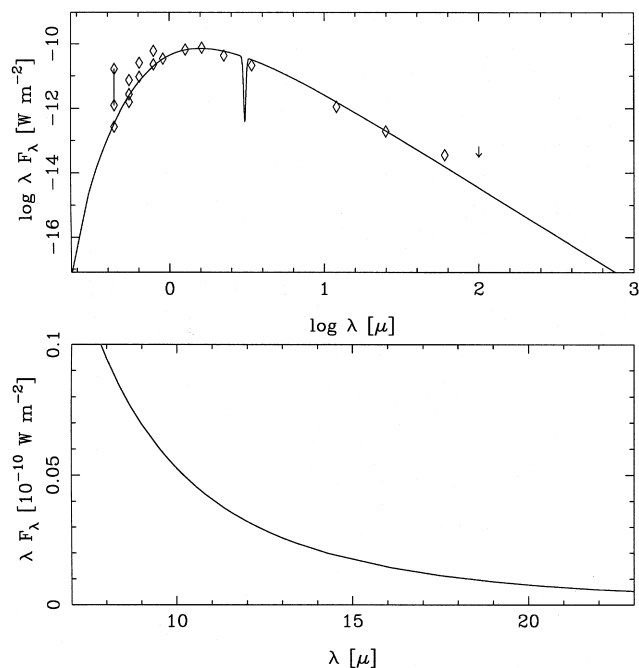


Figure 6. IRAS 03243 + 4400 (Y Per).

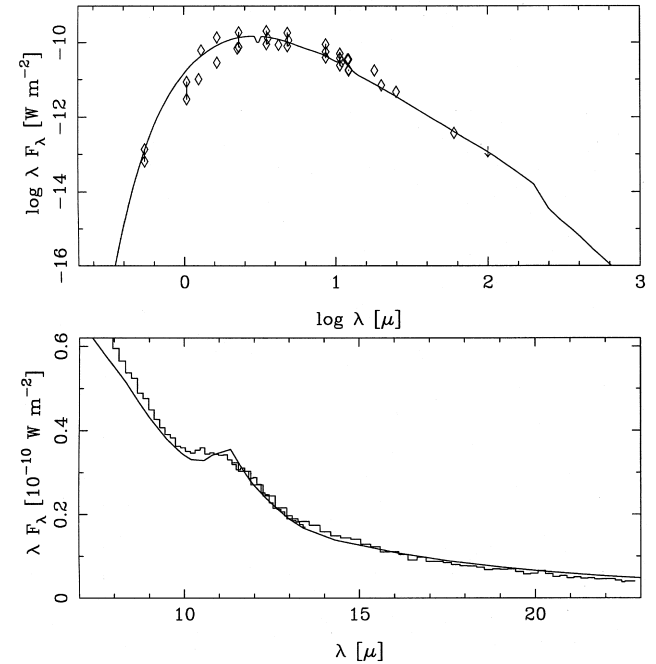


Figure 7. IRAS 03488 + 3943 (AFGL 527).

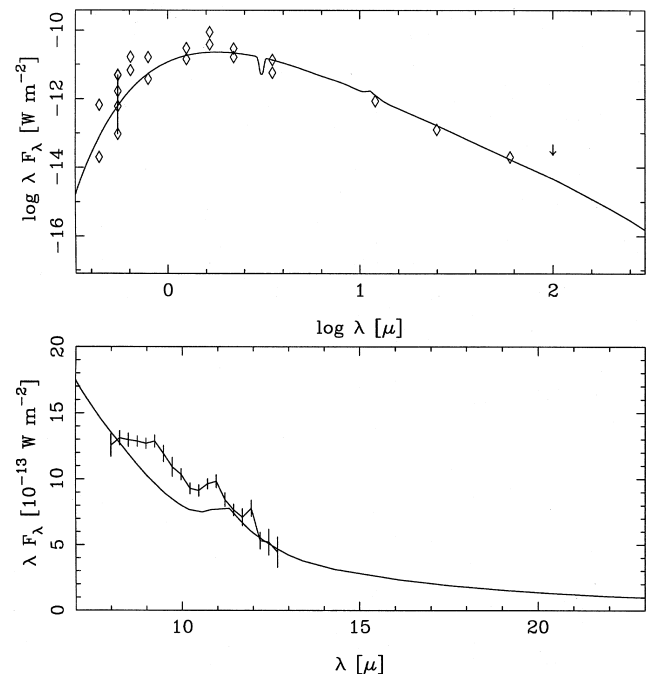


Figure 8. IRAS 04562 + 0803 (R Ori). The line with the error bars represents the AAT spectrum.

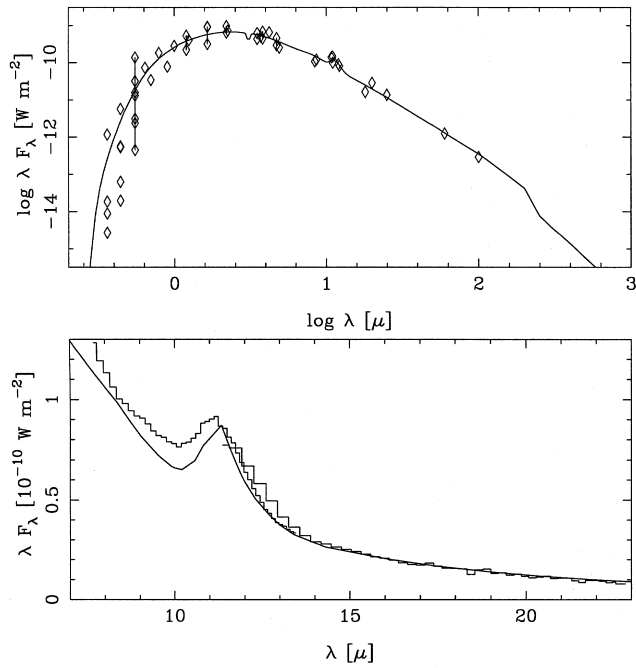


Figure 9. IRAS 04573 – 1452 (R Lep).

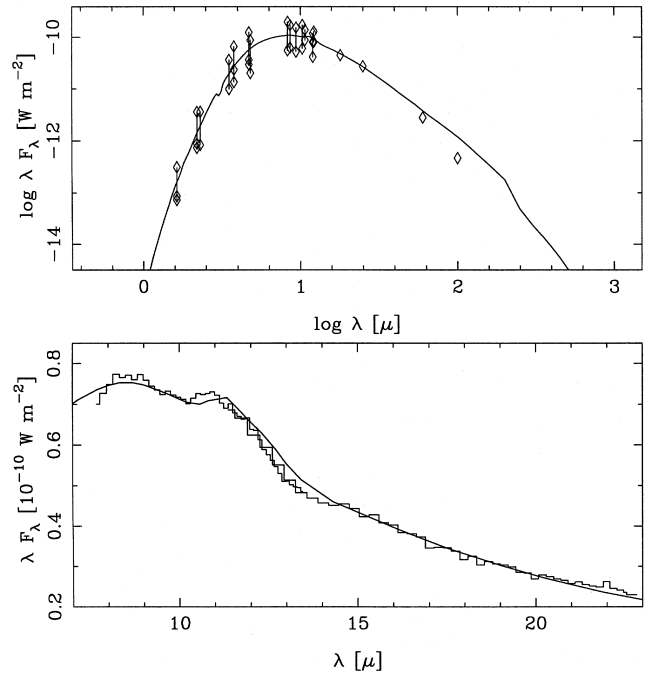
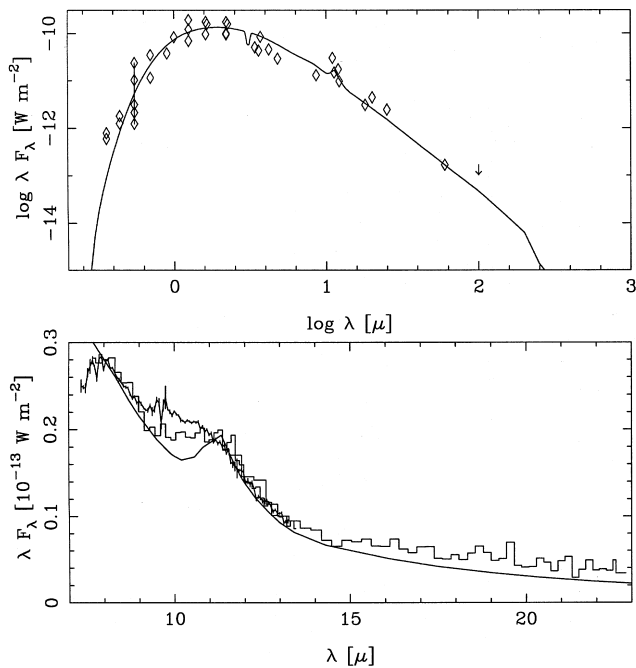
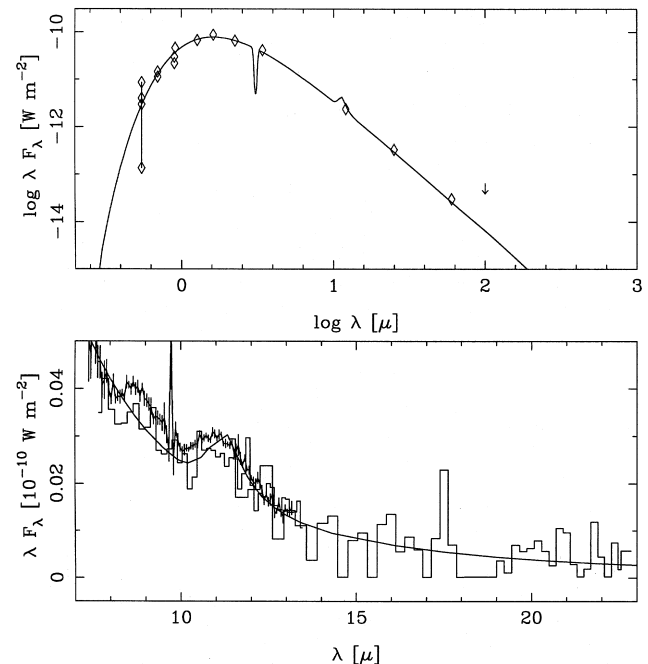


Figure 11. IRAS 06012 + 0328 (AFGL 865).


 Figure 10. IRAS 05185 + 3227 (UV Aur). The 8–13 μ m spectrum represents the UKIRT spectrum scaled by a factor of 1.8.

 Figure 12. IRAS 06202 + 4743 (V Aur). The 8–13 μ m spectrum represents the (unscaled) UKIRT spectrum.

489 (Fig. 5), R Lep (Fig. 9)]. A special case is that of the reddest stars, like AFGL 190 and 3068. There have been claims that the SiC feature goes into absorption (Jones et al. 1978; Lequeux & Jourdain de Muizon 1990; Justtanont et al. 1996) for such stars. For comparison, AFGL 3068 (Fig. 42) is fitted with pure AMC, while for AFGL 190 (Fig. 1) an attempt was made to fit the LRS spectrum with AMC plus SiC. It is clear that neither model fits well. There may be SiC

present in both circumstellar shells, but apparently the standard absorption coefficient, which is very successful in explaining most other observed features, does not work here. Note that in other stars which have comparably large optical depths [e.g., AFGL 865 (Fig. 11), AFGL 2494 (Fig. 33), or AFGL 2513 (Fig. 34)] a small fraction of SiC is required to obtain good fits to the LRS spectra.

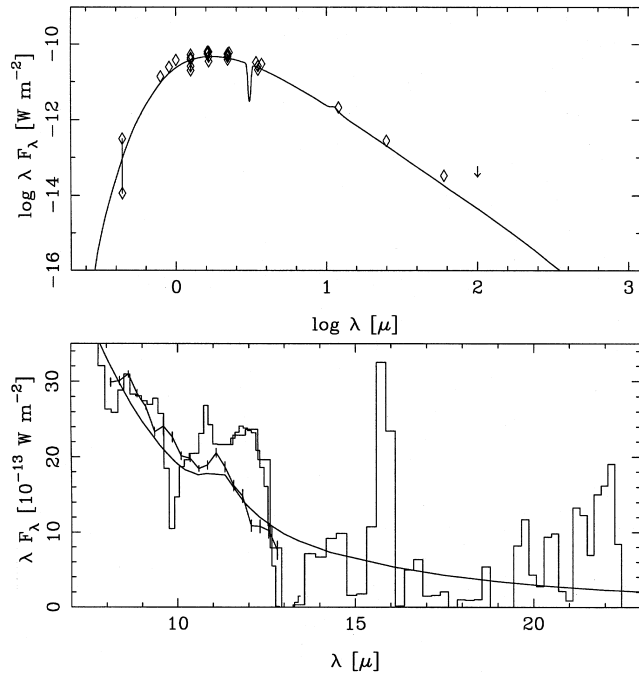


Figure 13. IRAS 06209 + 2503 (ZZ Gem). The 8–13 μm spectrum represents the (unscaled) AAT spectrum.

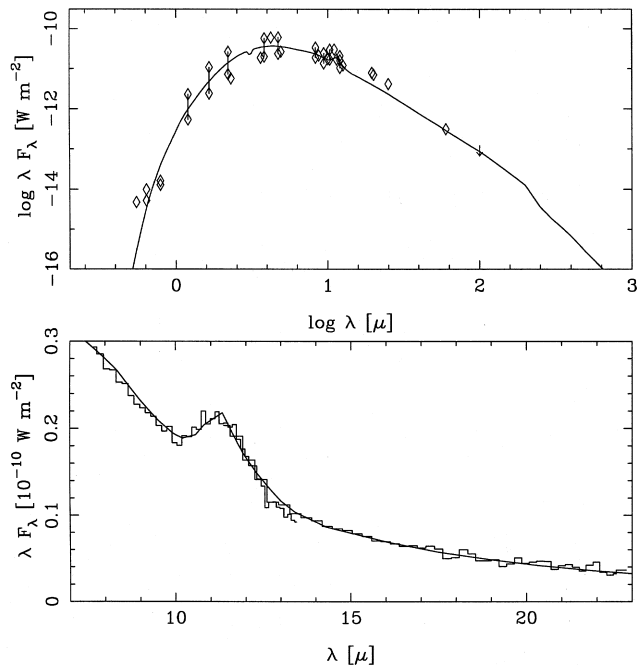


Figure 14. IRAS 06230 – 0930 (AFGL 935).

6 THE TOTAL MASS-LOSS RATE AND DUST-TO-GAS RATIO

From the radiative transfer modelling the dust mass-loss rate has been derived. The values listed in Table 3 assume an opacity at 60 μm of $68 \text{ cm}^2 \text{ g}^{-1}$ and a dust velocity equal to the gas velocity. In this section the total mass-loss rate, the correction for the drift velocity, and the dust-to-gas ratio are estimated.

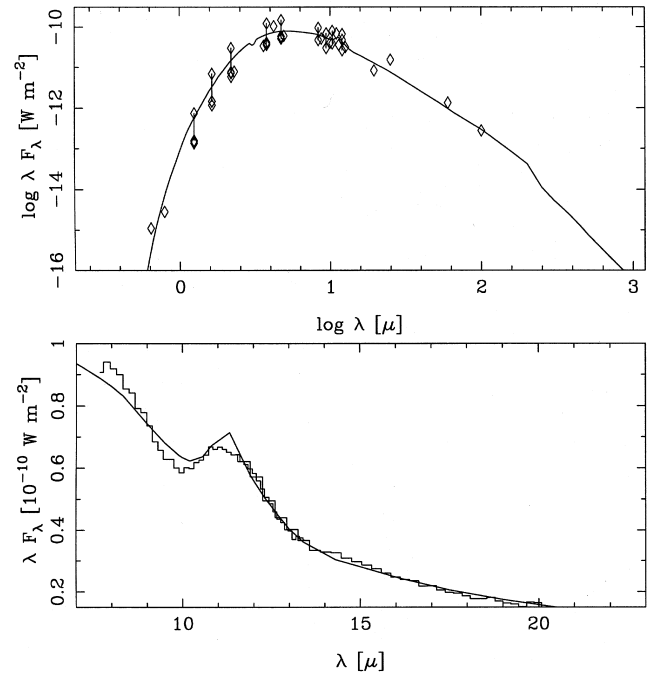


Figure 15. IRAS 06342 – 0328 (AFGL 971).

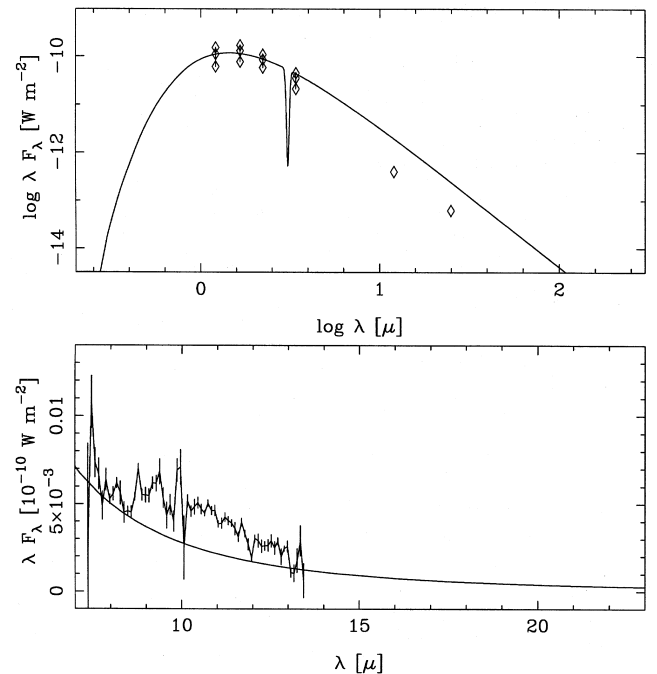


Figure 16. IRAS 06436 + 1840 (RT Gem). The 8–13 μm spectrum represents the (unscaled) UKIRT spectrum.

The gas mass-loss rate can be derived, e.g., from CO observations. In a parallel study we have obtained new CO observations and their analyses will be presented in a separate paper. Here, the total mass-loss rate will be derived from equations similar to those in Ivezić & Elitzur (1995) and Netzer & Elitzur (1993), which are exact if radiation pressure is the force that drives the outflow (also see Appendix A):

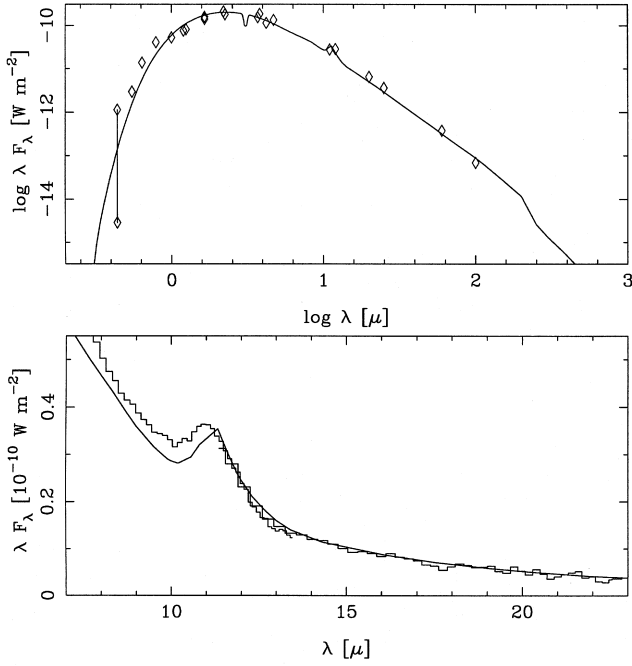


Figure 17. IRAS 06529 + 0626 (CL Mon).

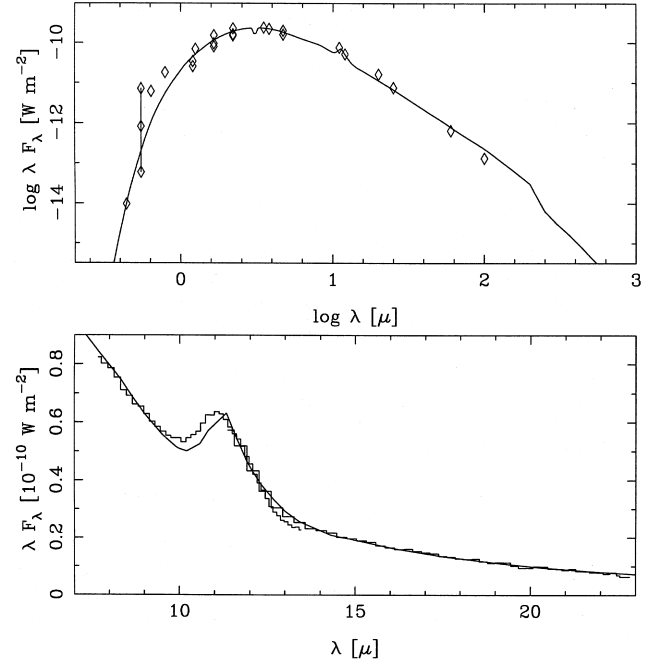


Figure 19. IRAS 07065 - 7256 (R Vol).

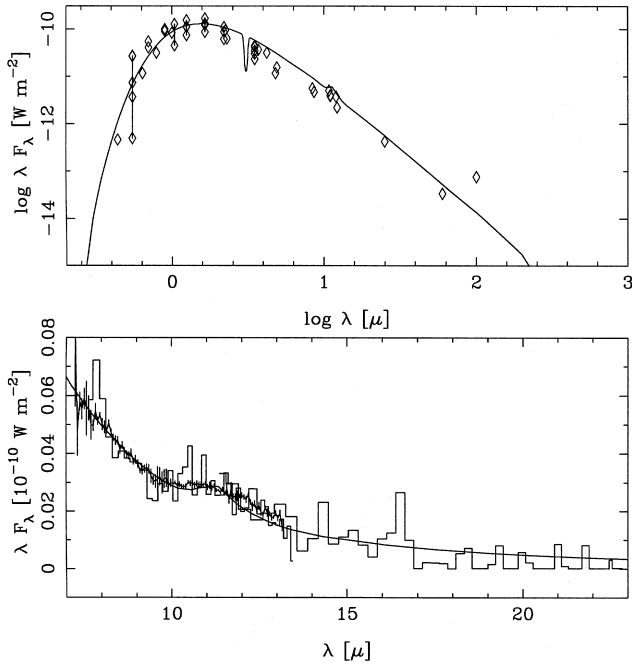
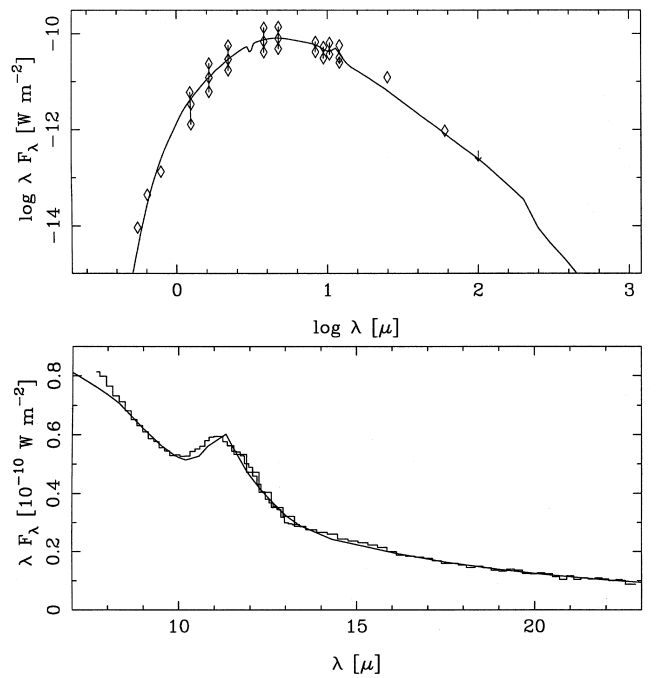

 Figure 18. IRAS 07059 + 1006 (R CMi). The 8–13 μm spectrum represents the UKIRT spectrum scaled by a factor of 0.75.


Figure 20. IRAS 07098 - 2012 (AFGL 1085).

$$\dot{M} = 2.02 \times 10^{-8} \tau_F \frac{L}{v_\infty - v_0} \left(1 - \frac{1}{\Gamma}\right) M_\odot \text{ yr}^{-1}, \quad (5)$$

where τ_F is the flux-weighted optical depth at infinity, L is the luminosity in solar units, v_∞ is the terminal gas velocity, v_0 is the gas velocity, in km s^{-1} , at the dust condensation radius, and Γ is the ratio of radiation pressure to gravitational pull. The mass-loss rate can be derived when Γ is

known. Its relation to physical quantities can be written down exactly (see Appendix A), but it is then in a form which is not suitable for practical calculations. In Appendix A an approximation is made which leads to the following form:

$$\Gamma = \frac{3Q_F(\infty)L\Psi}{16\pi a \rho_d c G M_*} \frac{v_\infty}{v_\infty + v_{\text{drift}}}, \quad (6)$$

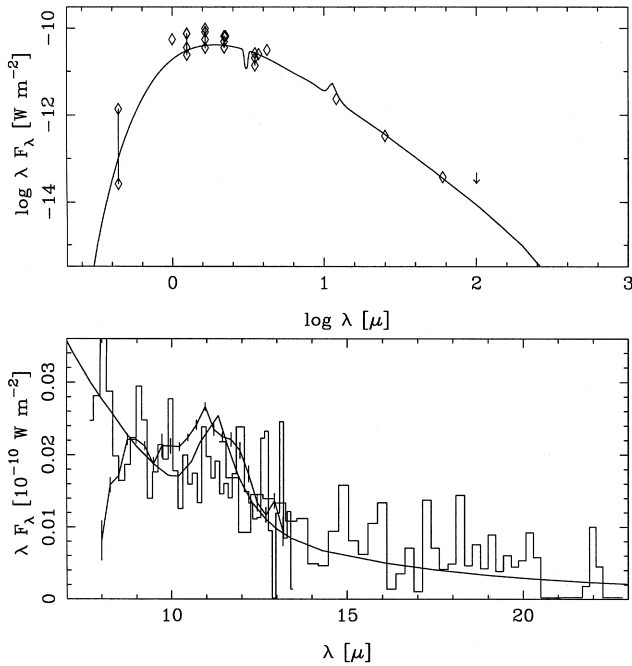


Figure 21. IRAS 07099 + 1441 (VX Gem). The 8–13 μm spectrum represents the AAT observations scaled by a factor of 1.5.

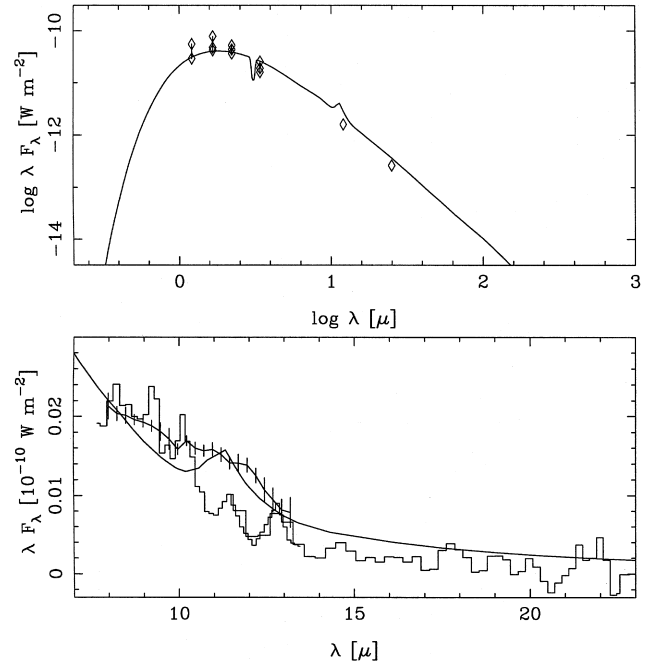


Figure 23. IRAS 10324 – 5358 (TV Vel). The 8–13 μm spectrum represents the AAT observations scaled by a factor of 0.66.

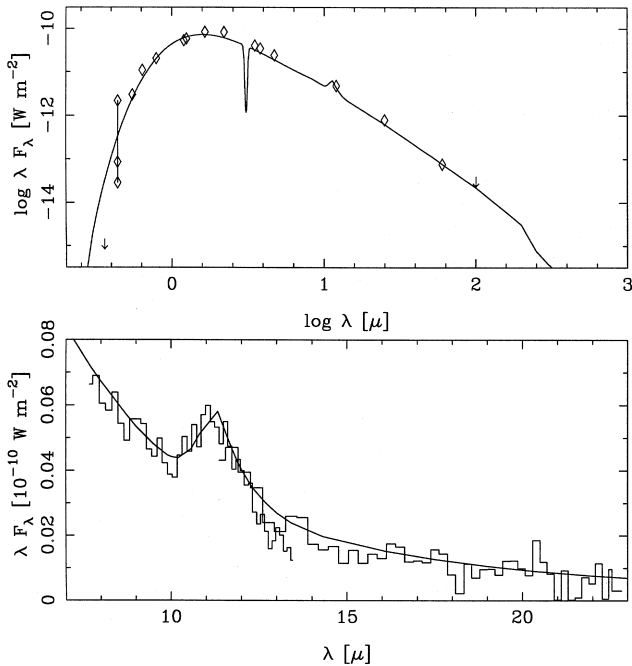


Figure 22. IRAS 08434 – 2801 (R Pyx).

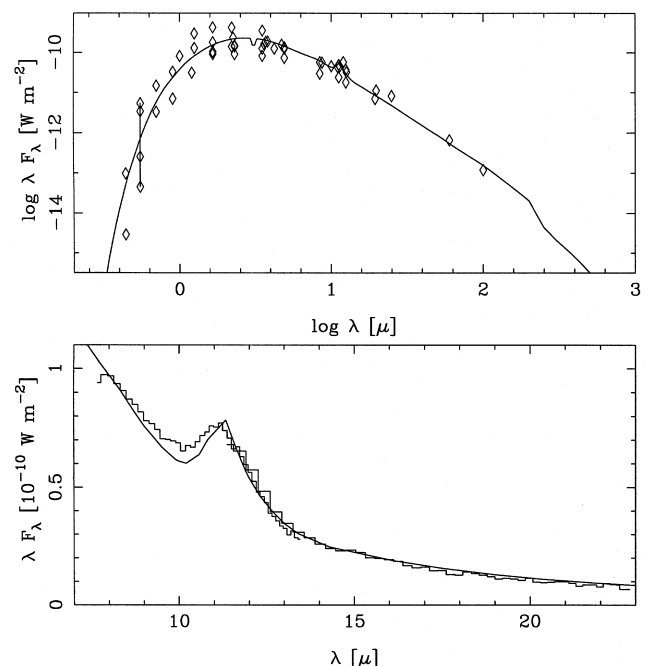


Figure 24. IRAS 12447 + 0425 (RU Vir).

where c is the speed of light, G is the gravitational constant, and M_* is the mass of the star; the other symbols have been defined previously. This approximation should yield accurate results when Γ is large, so its precise value does not influence the derivation of the mass-loss rate. For small values of Γ the accuracy may be less, but the results should still be more realistic than those obtained by assuming that Γ is large.

We also define a quantity y_0 as follows:

$$y_0 \equiv 1 - \left(\frac{v_0^2}{v_\infty^2 - v_0^2} \right) \quad (7)$$

and

$$Y \equiv 2 (1 - \sqrt{1 - y_0}) / y_0. \quad (8)$$

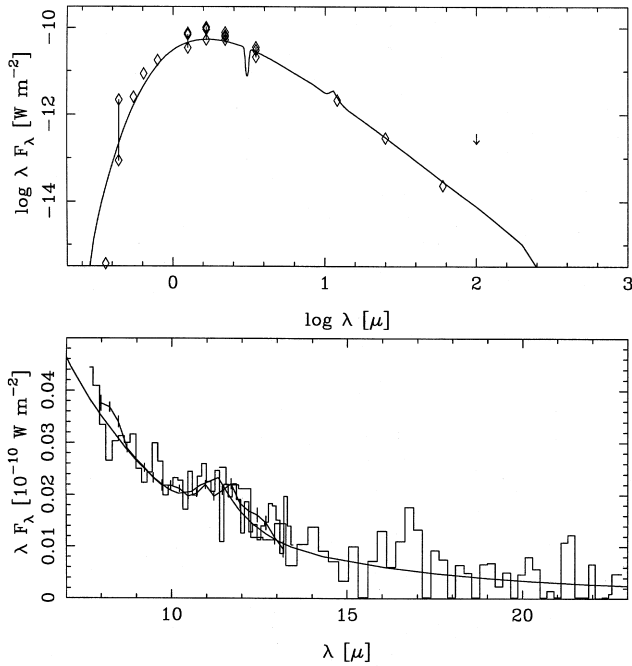


Figure 25. IRAS 12536 – 5737 (V Cru).

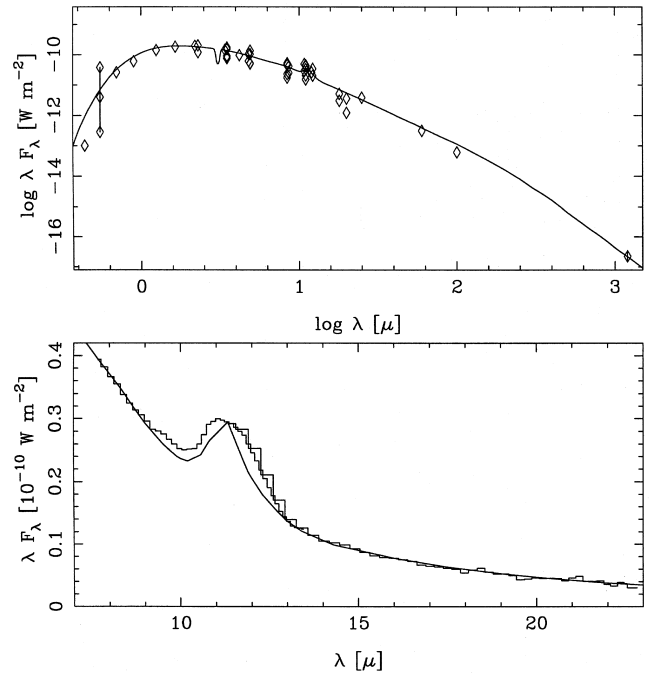


Figure 27. IRAS 15477 + 3943 (V CrB).

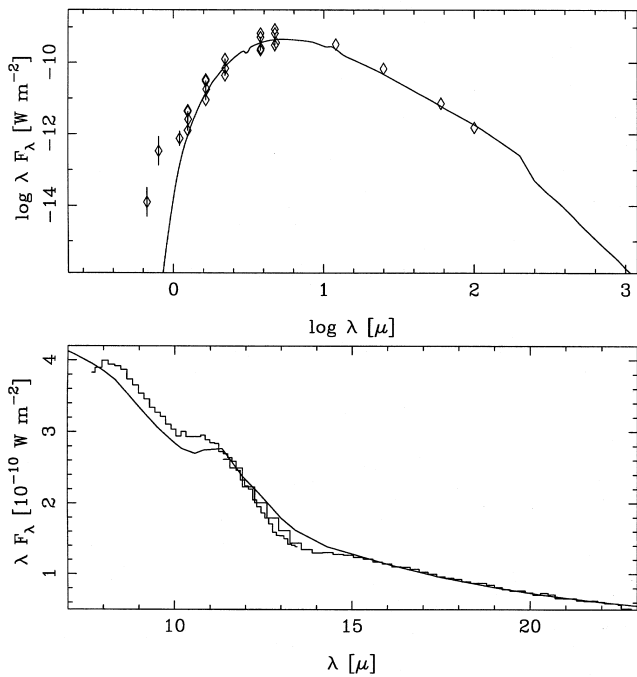


Figure 26. IRAS 15194 – 5115.

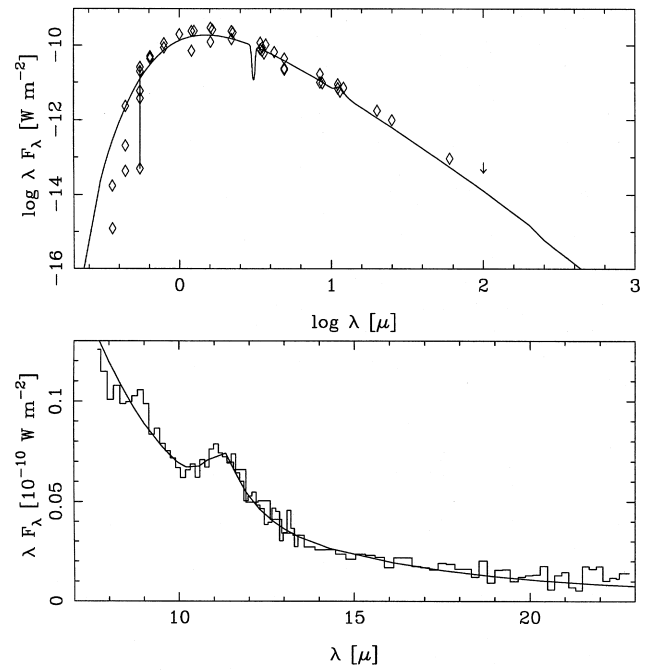


Figure 28. IRAS 16239 – 1218 (V Oph).

The derivation of the mass-loss rate and dust-to-gas ratio then proceeds as follows.

(i) Choose values for the grain size (a), the opacity at 60 μm (κ), the mass of the star (M_*), and the gas velocity (v_0) at the condensation point. Calculate the effective absorption coefficient by multiplying the value in Table 3 by $(a/0.1 \times \kappa/68)$, and the dust mass-loss rate by multiplying the value in Table 3 by $(\kappa/68)$, and divide by Y (equation 8) to

get the first-order correction for the effect of the dust velocity law (this is explained in Appendix A). Initially set Γ to a large value.

(ii) Calculate the mass-loss rate using equation (5) with the values of L , v_∞ and τ_F from Tables 2 and 3.

(iii) Calculate the drift velocity (v_{drift}) from equation (2).

(iv) Calculate the dust mass-loss rate, by multiplying the value found under step (i) by $(v_\infty + v_{\text{drift}})/v_\infty$, and then the resulting dust-to-gas ratio (Ψ).

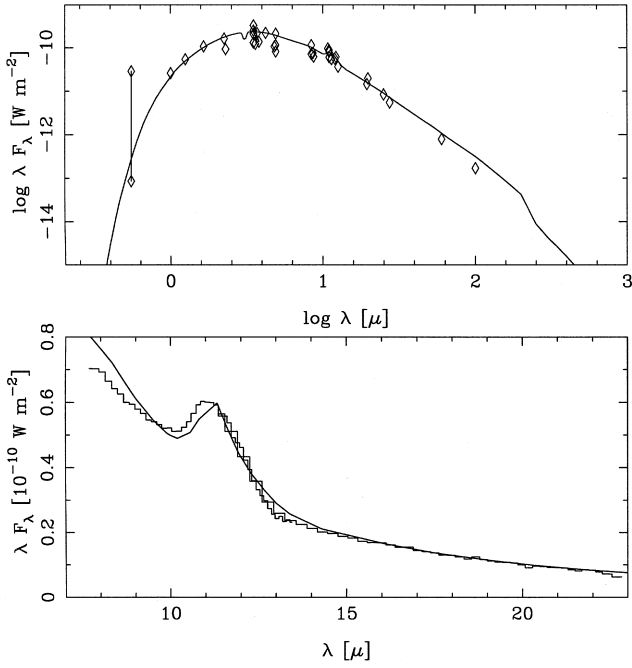


Figure 29. IRAS 17556 + 5813 (T Dra).

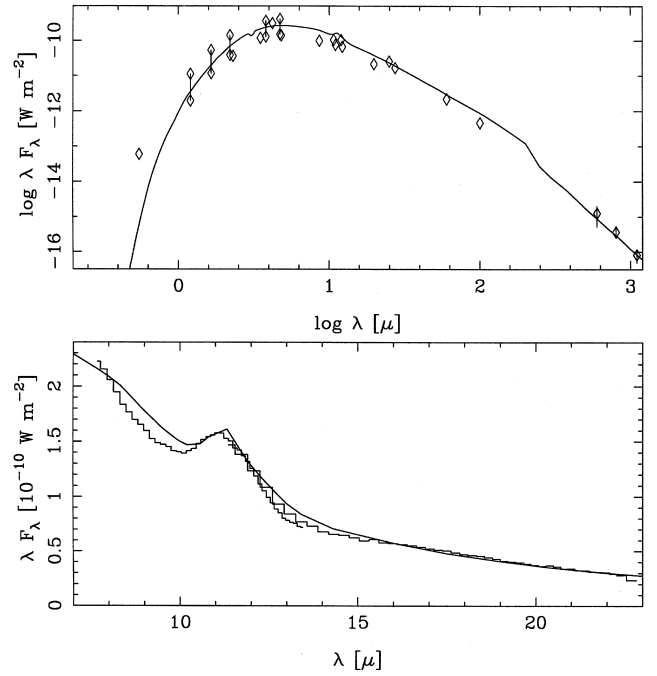


Figure 31. IRAS 19175 - 0807 (AFGL 2368).

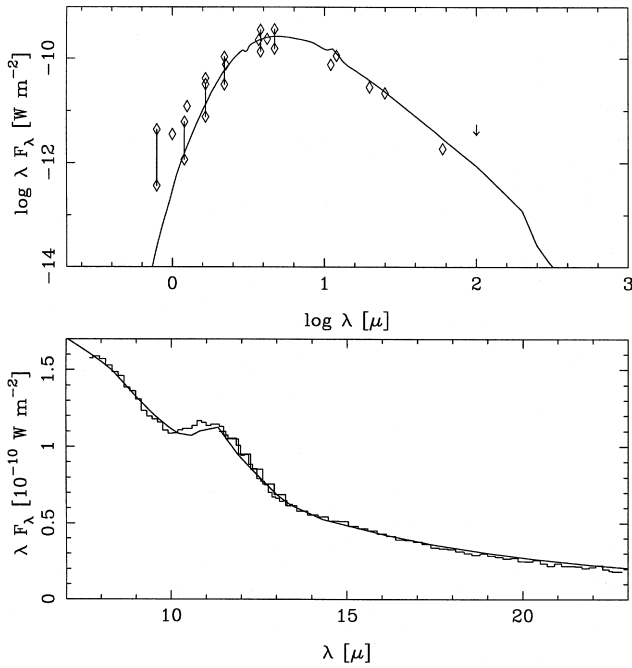


Figure 30. IRAS 19008 + 0726 (AFGL 2310).

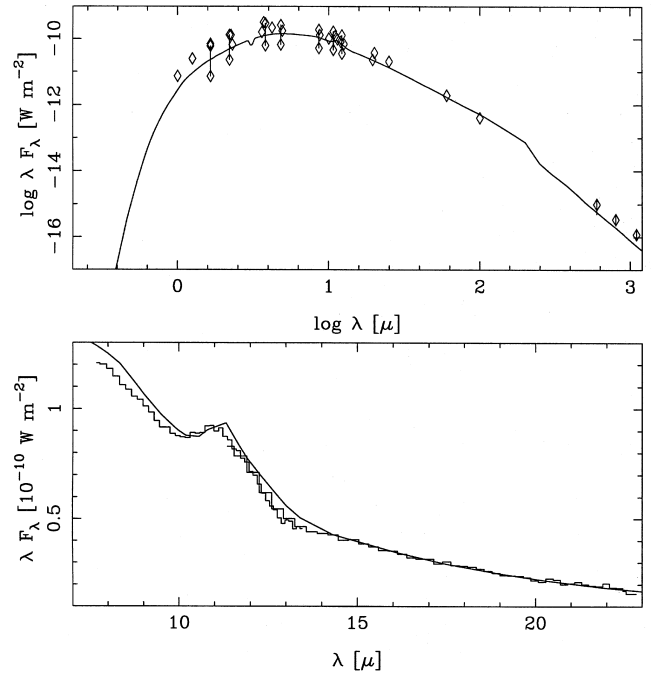


Figure 32. IRAS 19321 + 2757 (AFGL 2417).

(v) Calculate Γ from equation (6).

(vi) Go to step (ii), and iterate until the value of Γ has converged.

This procedure can be followed for all stars, except those without detected gas expansion velocity, and those for which no dust mass-loss rate could be derived.

Models have been run using this procedure for five different sets of parameters: model A, with the default param-

eters $a=0.1 \mu\text{m}$, $\kappa_{60}=68 \text{ cm}^2 \text{ g}^{-1}$, $M_* = 0.6 M_\odot$, $v_0 = 1 \text{ km s}^{-1}$, and models with $a=0.01 \mu\text{m}$ (model B), $\kappa_{60}=150 \text{ cm}^2 \text{ g}^{-1}$ (model C), $M_* = 0.8 M_\odot$ (model D) and $v_0 = 3 \text{ km s}^{-1}$ (model E). The results are collected in Table 4, where the mass-loss rate, the dust-to-gas ratio, Γ and the drift velocity are listed.

The effect of lowering the grain size is primarily to lower Q , as Q/a is approximately constant. This reduces the drift

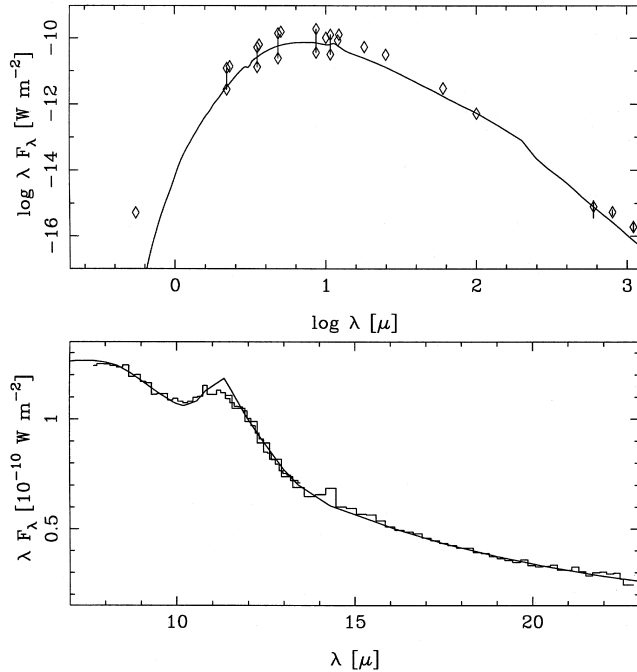


Figure 33. IRAS 19594 + 4047 (AFGL 2494).

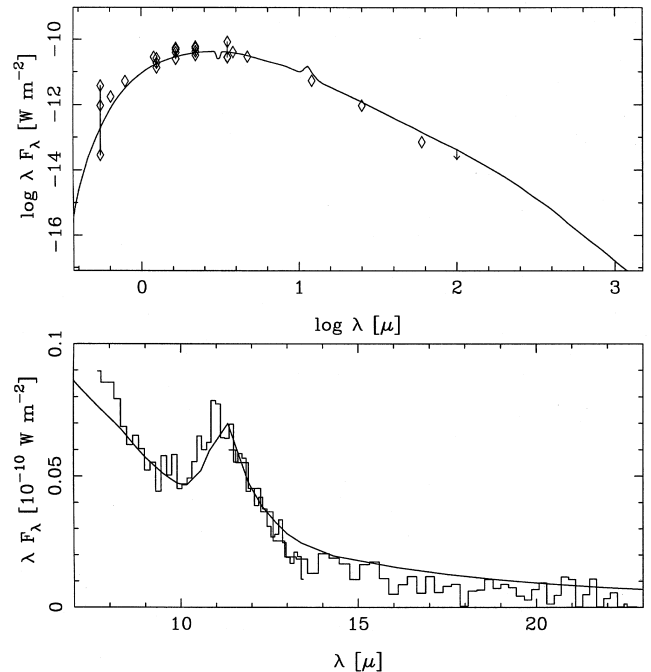


Figure 35. IRAS 20085 - 1425 (R Cap).

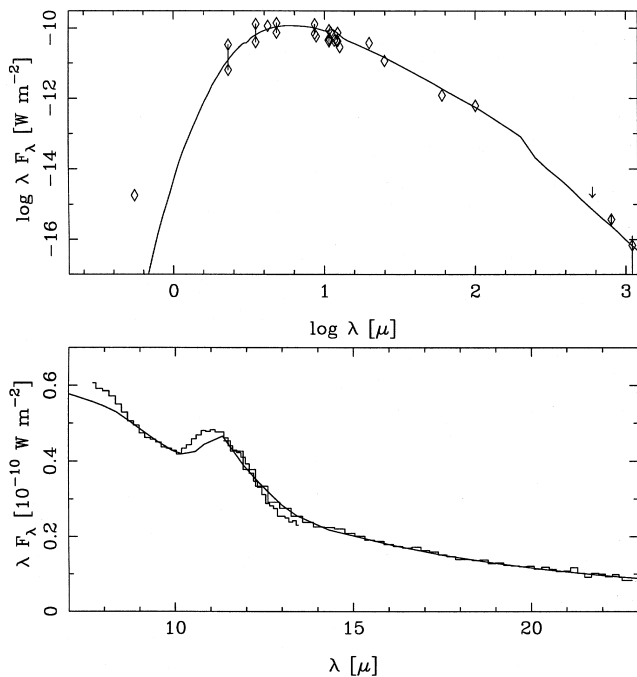


Figure 34. IRAS 20072 + 3116 (AFGL 2513).

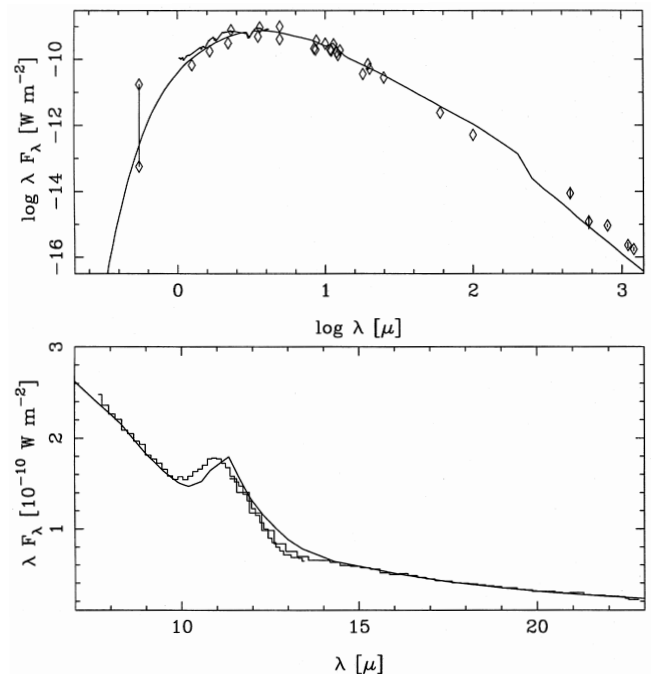


Figure 36. IRAS 20396 + 4757 (V Cyg).

velocity. The dust mass-loss rate, and hence Ψ , change slightly due to the different drift velocity. Γ remains constant, however, as the same term with the drift velocity ($v_\infty + v_{\text{drift}}$) appears in equation (6). The effect of increasing κ_{60} is first of all to increase Q . This leads to higher drift velocities. A second effect is that the dust mass-loss rate (even apart from the change in the drift velocity) must decrease, to keep the optical depth constant (equation 1). Γ

remains constant, as the direct effects of the change in Q and Ψ cancel, as well as the secondary effect due to the change in v_{drift} . The effect of increasing M_* is to lower Γ , which lowers the mass-loss rate, which in turn changes the drift velocity and Ψ . The effect of increasing v_0 is to increase the mass-loss rate, which in turn affects all other parameters.

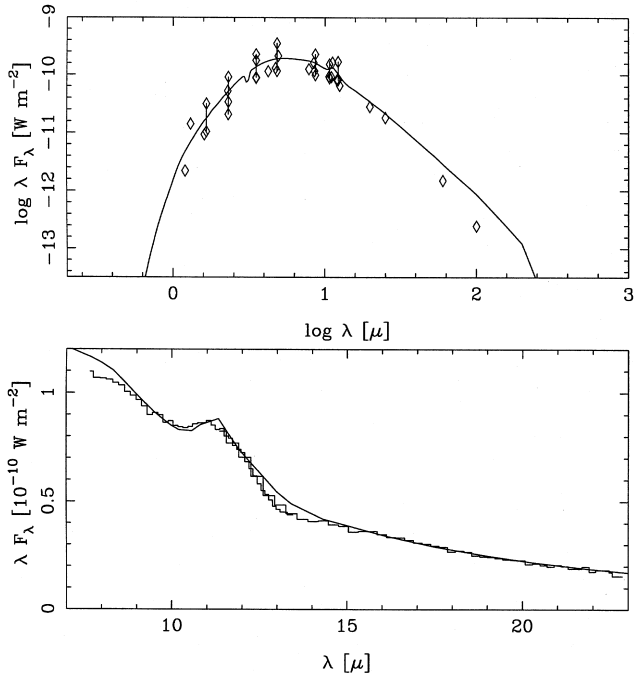


Figure 37. IRAS 20570 + 2714 (AFGL 2686).

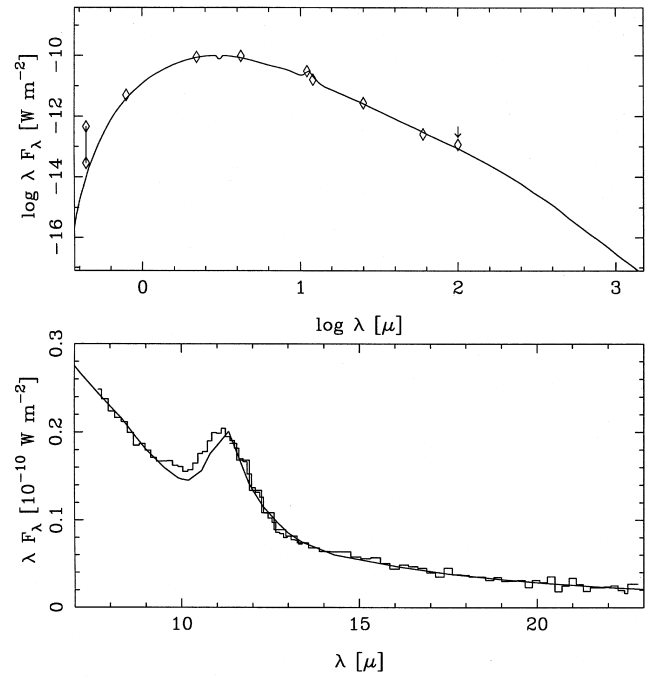


Figure 39. IRAS 21262 + 7000 (AX Cep).

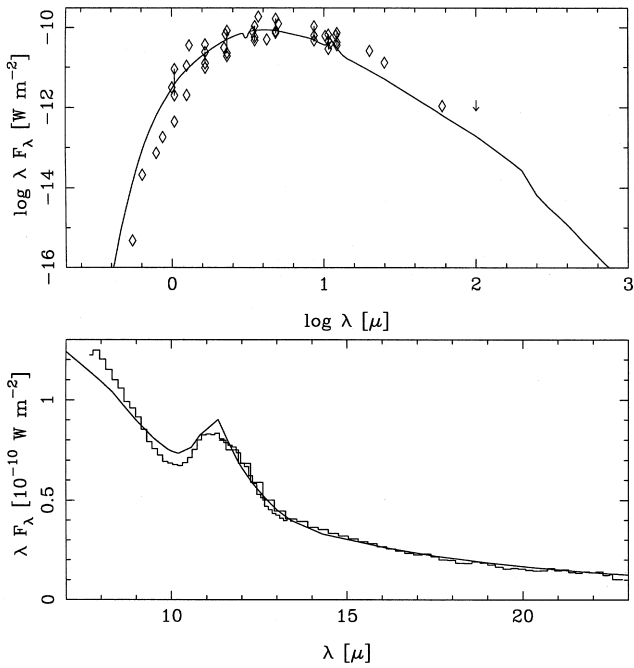


Figure 38. IRAS 21035 + 5136 (AFGL 2704).

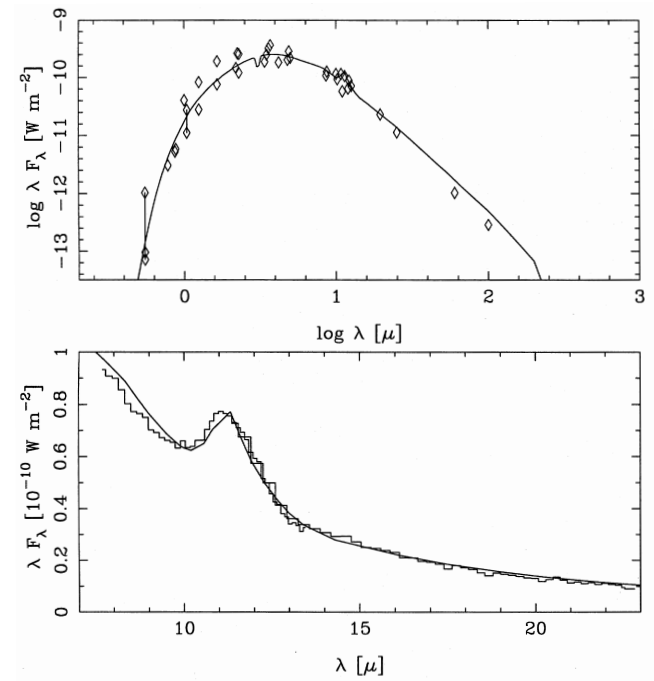


Figure 40. IRAS 21320 + 3850 (AFGL 2781).

7 DISCUSSION

7.1 Mass-loss rate and dust-to-gas ratio

In Fig. 44 the mass-loss rates and dust-to-gas ratios as derived from model A in Table 4 are plotted against pulsation period and luminosity (the filled squares). There is a good correlation between $\log \dot{M}$ and $\log L$ and $\log P$ over the entire range. Least-squares fitting on the 36 data points gives the following results:

$$\log \dot{M} = (4.08 \pm 0.41) \log P - (16.54 \pm 1.10) \quad \sigma = 0.27, \quad (9)$$

and

$$\log \dot{M} = (3.94 \pm 0.28) \log L - (20.79 \pm 1.10) \quad \sigma = 0.28. \quad (10)$$

The results for models B–E are insignificantly different. As we assumed a P – L relation from the start, these relations are not independent. If we had assumed a constant lumino-

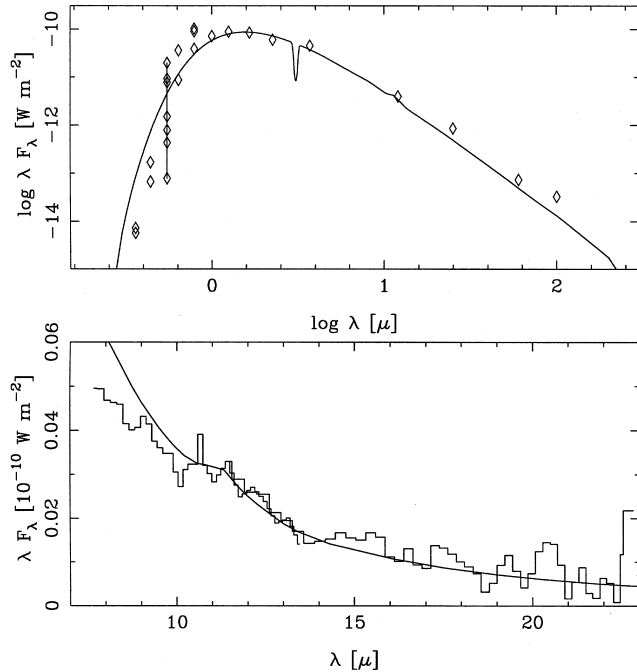


Figure 41. IRAS 22036 + 3315 (RZ Peg).

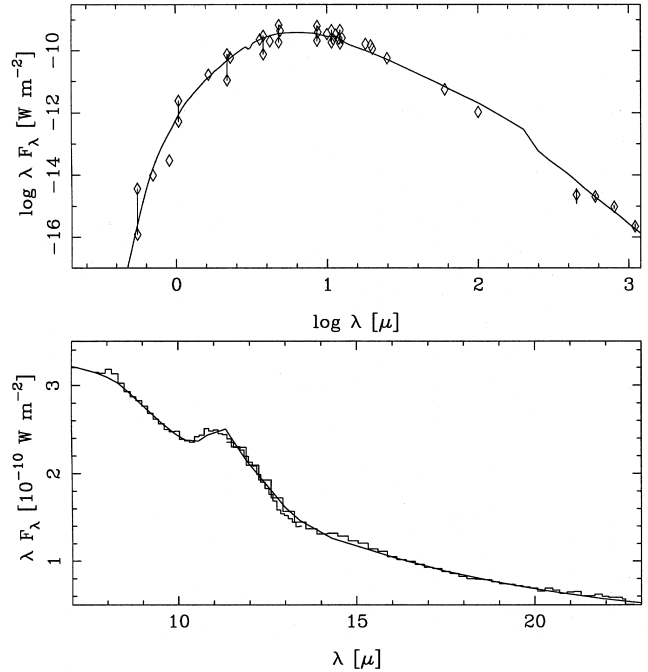


Figure 43. IRAS 23320 + 4316 (AFGL 3116).

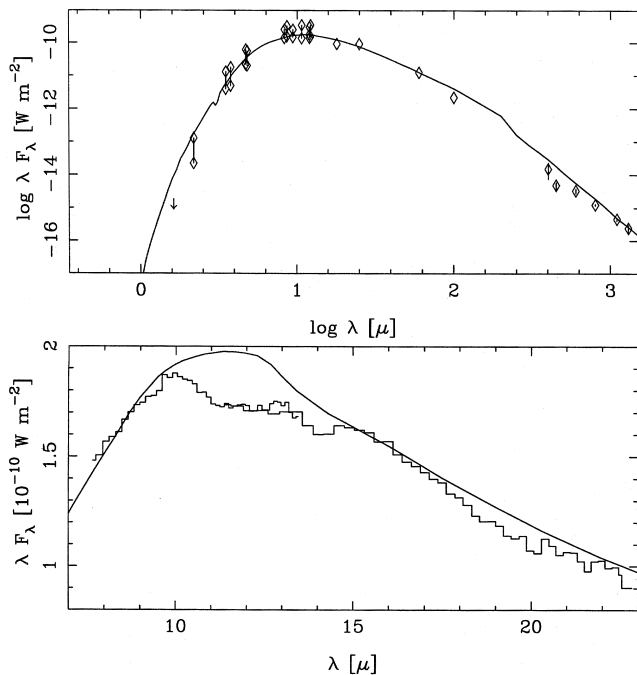


Figure 42. IRAS 23166 + 1655 (AFGL 3068).

sity for all stars, we still would have found a significant relation between mass-loss rate and pulsation period.

Whitelock (1990) and Whitelock et al. (1994) derived the mass-loss rates for oxygen-rich Miras in the Galactic Bulge and at high galactic latitude, respectively. The dashed polygon in Fig. 44 indicates the region wherein most of the former sample is located, while the dotted polygon indicates the region wherein most of the latter sample is located.

The relations for oxygen-rich and carbon Miras appear to be similar. There are some caveats, however. The mass-loss rates for the oxygen-rich Miras were not derived from model fits to the SEDs, but from Jura's (1987) formula which relates mass-loss rate to the *IRAS* flux, luminosity, mean wavelength of the emergent light, dust-to-gas ratio and expansion velocity. Whitelock assumed a constant dust-to-gas ratio and a constant expansion velocity for all of the stars in a given sample. As we show below, the dust-to-gas ratio for carbon stars appears to be a function of period, and there is a large spread in expansion velocity at a given period. If the same holds for oxygen-rich stars, then there will be systematic uncertainties in the derived mass-loss rates of the two samples of oxygen-rich Miras.

The dust-to-gas ratio appears to be rather constant at a value of 0.0025 up to $P \approx 500$ d, or $L \approx 7900 L_{\odot}$, and then to increase markedly to values up to 0.015. AFGL 3068 appears to have an extremely high dust-to-gas ratio of about 0.02. The absolute values of the derived ratio depend somewhat on the model (see Table 4), but the trend remains the same.

Fig. 45 shows the relation between the mass-loss rate and the amplitude of variability in the *K* band. As is well known, larger amplitude implies larger mass-loss rate. A least-squares fit, excluding the open symbols which represent the stars for which no mass-loss rate could be derived, and the two stars at $\dot{M} \approx 10^{-7} M_{\odot} \text{ yr}^{-1}$, is

$$\log \dot{M} = (0.62 \pm 0.07) \Delta K - (6.12 \pm 0.10) \quad \sigma = 0.14. \quad (11)$$

A similar plot for oxygen-rich Miras was shown by Whitelock (1990) and Whitelock et al. (1994) for the samples of oxygen-rich stars discussed above. The dashed polygon indicates the region within which most of the Galactic bulge stars are located, and the dotted polygon the region within which most of the high-latitude Miras are located. There is considerable overlap between these regions.

Table 3. The fitted parameters.

| IRAS-name | T_{inn} (K) | T_{eff} (K) | $\dot{M}_{\text{dust}}^{(a)}$ ($M_{\odot} \text{ yr}^{-1}$) | r_c (R_{\ast}) | $x^{(b)}$ | d (kpc) | $\tau_{11.33}$ | $\tau_{0.5}$ | τ_F | $Q_F^{(c)}$ | remarks |
|------------|-------------------------|-------------------------|--|-------------------------|-----------|--------------|----------------|--------------|----------|-------------|------------------------|
| 01144+6658 | 1000 | 2500 | $9.5 \cdot 10^{-7}$ | 9.8 | 0.08 | 3.99 | 4.84 | 79.2 | 2.41 | 0.0115 | AFGL 190 |
| 02032+5636 | 1500 | 2500 | $1.0 \cdot 10^{-9}$ | 2.0 | 0.08 | 3.09 | 0.076 | 1.24 | 0.29 | 0.0884 | |
| 02270-2619 | 1300 | 2300 | $4.9 \cdot 10^{-9}$ | 2.4 | 0.04 | 0.60 | 0.12 | 2.60 | 0.45 | 0.0665 | AFGL 337 |
| 02293+5749 | 1000 | 2500 | $3.0 \cdot 10^{-7}$ | 8.3 | 0.08 | 2.55 | 2.62 | 42.9 | 1.74 | 0.0152 | AFGL 341 |
| 03229+4721 | 1000 | 2500 | $2.5 \cdot 10^{-8}$ | 6.0 | 0.06 | 0.65 | 0.31 | 5.75 | 0.63 | 0.0408 | AFGL 489 |
| 03243+4400 | - | 2500 | 0.0 | - | - | 1.04 | 0.0 | 0.0 | 0.0 | 0.1211 | \dot{M} forced to 0 |
| 03488+3943 | 1500 | 2500 | $1.2 \cdot 10^{-8}$ | 2.2 | 0.04 | 0.99 | 0.18 | 3.93 | 0.62 | 0.0608 | AFGL 527 |
| 04562+0803 | 1500 | 2500 | $6.0 \cdot 10^{-10}$ | 2.0 | 0.05 | 2.22 | 0.038 | 0.86 | 0.20 | 0.1000 | |
| 04573-1452 | 1500 | 3000 | $4.2 \cdot 10^{-9}$ | 3.3 | 0.08 | 0.42 | 0.14 | 2.31 | 0.49 | 0.0789 | AFGL 667 |
| 05185+3227 | 1500 | 3000 | $1.0 \cdot 10^{-9}$ | 3.1 | 0.06 | 0.85 | 0.061 | 1.15 | 0.32 | 0.1025 | AFGL 735 |
| 06012+0328 | 800 | 2500 | $2.4 \cdot 10^{-7}$ | 12.0 | 0.02 | 1.45 | 0.89 | 23.2 | 1.06 | 0.0173 | AFGL 865 |
| 06202+4743 | 1500 | 2500 | $3.0 \cdot 10^{-10}$ | 1.9 | 0.25 | 1.16 | 0.025 | 0.18 | 0.058 | 0.1029 | |
| 06209+2503 | 1500 | 2500 | $8.5 \cdot 10^{-11}$ | 1.9 | 0.10 | 1.32 | 0.013 | 0.20 | 0.057 | 0.1130 | |
| 06230-0930 | 1200 | 2500 | $2.7 \cdot 10^{-8}$ | 4.1 | 0.05 | 2.00 | 0.43 | 8.71 | 0.85 | 0.0362 | AFGL 935 |
| 06342+0328 | 1100 | 2500 | $4.2 \cdot 10^{-8}$ | 5.3 | 0.05 | 1.55 | 0.58 | 11.7 | 0.90 | 0.0294 | AFGL 971 |
| 06436+1840 | - | 2800 | 0.0 | - | - | 0.91 | 0.0 | 0.0 | 0.0 | 0.1319 | \dot{M} forced to 0 |
| 06529+0626 | 1500 | 2500 | $4.7 \cdot 10^{-9}$ | 2.1 | 0.08 | 0.82 | 0.12 | 1.89 | 0.40 | 0.0790 | AFGL 1038 |
| 07059+1006 | 1500 | 2700 | $2.0 \cdot 10^{-10}$ | 2.3 | 0.08 | 0.86 | 0.016 | 0.27 | 0.086 | 0.1176 | |
| 07065-7256 | 1400 | 2500 | $1.1 \cdot 10^{-8}$ | 2.6 | 0.07 | 0.75 | 0.26 | 4.55 | 0.67 | 0.0544 | AFGL 4070 |
| 07098-2012 | 1000 | 2500 | $6.0 \cdot 10^{-8}$ | 6.2 | 0.05 | 1.63 | 0.37 | 7.46 | 0.69 | 0.0353 | AFGL 1085 |
| 07099+1441 | 1500 | 2500 | $8.0 \cdot 10^{-10}$ | 2.0 | 0.15 | 1.62 | 0.087 | 0.96 | 0.25 | 0.0908 | |
| 08434-2801 | 600 | 2500 | $8.0 \cdot 10^{-10}$ | 19.2 | 0.12 | 1.20 | 0.0091 | 0.12 | 0.033 | 0.1000 | |
| 09452+1330 | 1075 | 2000 | $7.5 \cdot 10^{-8}$ | 4.5 | 0.03 | 0.15 | 0.62 | 84.8 | 0.97 | 0.0261 | $a = 0.16 \mu\text{m}$ |
| 10324-5358 | 1500 | 2700 | $6.5 \cdot 10^{-10}$ | 2.4 | 0.08 | 1.54 | 0.050 | 0.82 | 0.23 | 0.1023 | |
| 12447+0425 | 1500 | 2500 | $5.0 \cdot 10^{-9}$ | 2.2 | 0.08 | 0.75 | 0.21 | 3.51 | 0.59 | 0.0627 | AFGL 1579 |
| 12536-5737 | 1500 | 2700 | $3.0 \cdot 10^{-10}$ | 2.3 | 0.10 | 1.33 | 0.026 | 0.37 | 0.12 | 0.1133 | |
| 15194-5115 | 1050 | 2500 | $8.0 \cdot 10^{-8}$ | 7.1 | 0.02 | 0.63 | 0.41 | 67.8 | 0.80 | 0.0293 | $a = 0.10 \mu\text{m}$ |
| 15477+3943 | 1000 | 2500 | $1.5 \cdot 10^{-9}$ | 5.4 | 0.07 | 0.71 | 0.052 | 0.99 | 0.22 | 0.0920 | AFGL 5311 |
| 16239-1218 | 1500 | 2700 | $8.5 \cdot 10^{-11}$ | 2.3 | 0.15 | 0.68 | 0.015 | 0.17 | 0.057 | 0.1169 | AFGL 1859 |
| 17556+5813 | 1200 | 2500 | $9.5 \cdot 10^{-9}$ | 3.8 | 0.06 | 0.73 | 0.25 | 4.62 | 0.63 | 0.0503 | AFGL 2040 |
| 19008+0726 | 1200 | 2500 | $7.0 \cdot 10^{-8}$ | 4.4 | 0.03 | 0.81 | 0.53 | 12.7 | 0.98 | 0.0301 | AFGL 2310 |
| 19175-0807 | 1100 | 2500 | $8.0 \cdot 10^{-8}$ | 5.2 | 0.04 | 0.88 | 0.49 | 10.8 | 0.88 | 0.0308 | AFGL 2368 |
| 19321+2757 | 900 | 2500 | $7.0 \cdot 10^{-8}$ | 7.9 | 0.03 | 1.11 | 0.29 | 6.90 | 0.64 | 0.0352 | AFGL 2417 |
| 19594+4047 | 900 | 2500 | $2.0 \cdot 10^{-7}$ | 8.9 | 0.05 | 1.84 | 0.90 | 18.1 | 1.02 | 0.0208 | AFGL 2494 |
| 20072+3116 | 1200 | 2500 | $1.1 \cdot 10^{-7}$ | 4.7 | 0.05 | 1.20 | 0.95 | 19.2 | 1.23 | 0.0244 | AFGL 2513 |
| 20085-1425 | 1200 | 2500 | $3.9 \cdot 10^{-9}$ | 3.6 | 0.10 | 1.47 | 0.19 | 2.96 | 0.47 | 0.0645 | |
| 20396+4757 | 1200 | 2500 | $1.1 \cdot 10^{-8}$ | 3.8 | 0.06 | 0.40 | 0.29 | 5.24 | 0.71 | 0.0471 | AFGL 2632 |
| 20570+2714 | 900 | 2500 | $1.1 \cdot 10^{-7}$ | 8.1 | 0.03 | 1.08 | 0.39 | 9.20 | 0.72 | 0.0297 | AFGL 2686 |
| 21035+5136 | 1100 | 2500 | $1.5 \cdot 10^{-8}$ | 4.8 | 0.06 | 1.32 | 0.31 | 5.89 | 0.67 | 0.0422 | AFGL 2704 |
| 21262+7000 | 1500 | 3000 | $5.0 \cdot 10^{-9}$ | 3.5 | 0.08 | 1.05 | 0.24 | 4.28 | 0.63 | 0.0618 | AFGL 2768 |
| 21320+3850 | 1050 | 2500 | $1.5 \cdot 10^{-8}$ | 5.2 | 0.06 | 0.72 | 0.25 | 4.71 | 0.59 | 0.0467 | CIT 13 |
| 22036+3315 | 1200 | 2600 | $5.0 \cdot 10^{-10}$ | 3.7 | 0.03 | 1.23 | 0.011 | 0.28 | 0.085 | 0.1148 | |
| 23166+1655 | 650 | 2500 | $5.5 \cdot 10^{-7}$ | 20.4 | 0.00 | 1.15 | 1.12 | 36.0 | 1.11 | 0.0121 | AFGL 3068 |
| 23320+4316 | 900 | 2500 | $8.0 \cdot 10^{-8}$ | 8.5 | 0.03 | 0.71 | 0.55 | 13.0 | 0.84 | 0.0247 | AFGL 3116 |

(a) Dust mass rate assuming a dust opacity at $60 \mu\text{m}$ of $68 \text{ cm}^2 \text{ g}^{-1}$ and a dust velocity equal to the gas velocity.

(b) x is the mass ratio of SiC to AMC (see Section 2).

(c) For $a=0.1 \mu\text{m}$, and scales like $Q_F \sim a$.

For some stars, and some models, the drift velocities are larger than 20 km s^{-1} . This is the approximate limit where sputtering is thought to destroy dust grains (Salpeter 1977), although Krüger & Sedlmayr (1997) put the limit at 40 km s^{-1} . As can be seen from Table 4, and as discussed above, smaller grains than the default value of $0.1 \mu\text{m}$ make the drift velocity smaller. This has no influence on the mass-loss rate, and a small effect on the dust-to-gas ratios.

7.2 Expansion velocity

Fig. 46 shows the observed expansion velocity plotted versus luminosity and pulsation period. The correlation is poor. A similar result was found by Wood (1990) for oxygen-rich Miras, although he nevertheless had the courage to fit a straight line through his data points: the dotted line in Fig.

46. Lépine, Ortiz & Epchtein (1995) found a relatively good correlation for OH/IR stars with periods up to 700 d, shown as the dashed line in Fig. 46.

In order to make a more general comparison between oxygen-rich and carbon-rich Miras, we selected from the literature data on the CO and/or OH expansion velocities of oxygen-rich Miras and OH/IR stars with known periods. More details on the selection procedure can be found in Appendix B. The results are plotted as the dots in the bottom panel of Fig. 46.

There is a good deal of overlap between the regions occupied by oxygen-rich and carbon-rich stars, although for periods below 600 d the carbon stars appear to lie systematically above the oxygen-rich Miras. For large periods the expansion velocities seem to level off. For both oxygen- and carbon-rich stars there is a scatter of up to a factor of 2 in velocity at a given period.

Table 4. Final results.

| IRAS-name | $\dot{M}^{(b)}$ | \dot{M} | \dot{M} | $\Psi^{(c)}$ | Ψ | Ψ | Ψ | Ψ | Γ | Γ | Γ | $v_{dr}^{(d)}$ | v_{dr} | v_{dr} | v_{dr} | v_{dr} |
|----------------------|-----------------|-----------|-----------|--------------|--------|--------|--------|--------|----------|----------|----------|----------------|----------|----------|----------|----------|
| Model ^(a) | A,B,C | D | E | A | B | C | D | E | A,B,C | D | E | A | B | C | D | E |
| 01144+6658 | 42. | 41. | 48. | 1.3 | 1.2 | 0.59 | 1.3 | 1.2 | 10.8 | 8.3 | 10.5 | 1.3 | 0.4 | 1.9 | 1.3 | 1.2 |
| 02032+5636 | – | – | – | – | – | – | – | – | – | – | – | – | – | – | – | – |
| 02270–2619 | 2.0 | 1.7 | 2.2 | 0.20 | 0.15 | 0.10 | 0.23 | 0.19 | 2.5 | 2.1 | 2.4 | 8.2 | 2.6 | 12.2 | 8.8 | 7.7 |
| 02293+5749 | 27. | 26. | 32. | 0.65 | 0.61 | 0.31 | 0.69 | 0.63 | 5.4 | 4.3 | 5.2 | 1.4 | 0.5 | 2.1 | 1.5 | 1.3 |
| 03229+4721 | 5.3 | 4.9 | 6.1 | 0.32 | 0.27 | 0.16 | 0.35 | 0.31 | 4.0 | 3.2 | 3.9 | 4.4 | 1.4 | 6.6 | 4.6 | 4.1 |
| 03243+4400 | – | – | – | – | – | – | – | – | – | – | – | – | – | – | – | – |
| 03488+3943 | 2.7 | 2.5 | 2.8 | 0.31 | 0.26 | 0.16 | 0.34 | 0.31 | 5.3 | 4.2 | 5.3 | 10.6 | 3.3 | 15.7 | 10.9 | 10.2 |
| 04562+0803 | 0.67 | 0.55 | 0.81 | 0.11 | 0.069 | 0.065 | 0.15 | 0.10 | 1.4 | 1.3 | 1.3 | 13.1 | 4.1 | 19.4 | 14.5 | 11.9 |
| 04573–1452 | 2.1 | 1.9 | 2.4 | 0.16 | 0.12 | 0.083 | 0.18 | 0.15 | 2.5 | 2.1 | 2.5 | 9.6 | 3.0 | 14.3 | 10.2 | 9.1 |
| 05185+3227 | – | – | – | – | – | – | – | – | – | – | – | – | – | – | – | – |
| 06012+0328 | 13. | 12. | 15. | 1.1 | 1.0 | 0.53 | 1.2 | 1.1 | 8.7 | 6.8 | 8.5 | 2.2 | 0.7 | 3.2 | 2.2 | 2.0 |
| 06202+4743 | 0.18 | 0.16 | 0.20 | 0.24 | 0.14 | 0.14 | 0.29 | 0.23 | 2.3 | 2.0 | 2.2 | 35.0 | 11.1 | 51.9 | 37.4 | 33.2 |
| 06209+2503 | 0.10 | 0.077 | 0.13 | 0.23 | 0.11 | 0.15 | 0.35 | 0.21 | 1.1 | 1.1 | 1.1 | 26.8 | 8.5 | 39.8 | 31.0 | 23.9 |
| 06230–0930 | 5.6 | 5.1 | 6.4 | 0.31 | 0.27 | 0.15 | 0.34 | 0.30 | 3.2 | 2.7 | 3.2 | 4.0 | 1.3 | 6.0 | 4.2 | 3.8 |
| 06342+0328 | 10. | 9.1 | 12. | 0.27 | 0.24 | 0.13 | 0.30 | 0.26 | 3.2 | 2.6 | 3.1 | 2.8 | 0.9 | 4.2 | 3.0 | 2.6 |
| 06436+1840 | – | – | – | – | – | – | – | – | – | – | – | – | – | – | – | – |
| 06529+0626 | 1.8 | 1.6 | 1.9 | 0.20 | 0.16 | 0.11 | 0.23 | 0.20 | 3.9 | 3.1 | 3.8 | 13.3 | 4.2 | 19.7 | 13.9 | 12.8 |
| 07059+1006 | – | – | – | – | – | – | – | – | – | – | – | – | – | – | – | – |
| 07065–7256 | 3.2 | 2.9 | 3.6 | 0.23 | 0.19 | 0.12 | 0.26 | 0.22 | 3.1 | 2.5 | 3.0 | 6.9 | 2.2 | 10.3 | 7.3 | 6.6 |
| 07098–2012 | 6.0 | 5.8 | 6.6 | 0.64 | 0.56 | 0.32 | 0.67 | 0.63 | 9.8 | 7.6 | 9.7 | 5.6 | 1.8 | 8.4 | 5.7 | 5.4 |
| 07099+1441 | – | – | – | – | – | – | – | – | – | – | – | – | – | – | – | – |
| 08434–2801 | 0.33 | 0.30 | 0.43 | 0.40 | 0.22 | 0.24 | 0.45 | 0.34 | 3.5 | 2.9 | 3.3 | 17.2 | 5.4 | 25.5 | 18.0 | 15.0 |
| 09452+1330 | 11. | 10. | 13. | 0.44 | 0.39 | 0.21 | 0.48 | 0.42 | 4.5 | 3.6 | 4.3 | 2.6 | 0.8 | 3.9 | 2.7 | 2.4 |
| 10324–5358 | – | – | – | – | – | – | – | – | – | – | – | – | – | – | – | – |
| 12447+0425 | 2.6 | 2.3 | 3.0 | 0.15 | 0.12 | 0.76 | 0.18 | 0.14 | 2.0 | 1.7 | 1.9 | 7.0 | 2.2 | 10.3 | 7.5 | 6.5 |
| 12536–5737 | – | – | – | – | – | – | – | – | – | – | – | – | – | – | – | – |
| 15194–5115 | 5.9 | 5.7 | 6.5 | 0.85 | 0.75 | 0.42 | 0.88 | 0.83 | 8.7 | 6.8 | 8.6 | 4.4 | 1.4 | 6.6 | 4.5 | 4.2 |
| 15477+3943 | 1.2 | 1.0 | 1.6 | 0.13 | 0.089 | 0.076 | 0.17 | 0.12 | 1.6 | 1.5 | 1.5 | 8.0 | 2.5 | 12.0 | 8.9 | 7.1 |
| 16239–1218 | 0.099 | 0.075 | 0.12 | 0.24 | 0.11 | 0.15 | 0.36 | 0.22 | 1.1 | 1.1 | 1.1 | 27.2 | 8.6 | 40.5 | 31.4 | 24.3 |
| 17556+5813 | 3.6 | 3.1 | 4.2 | 0.20 | 0.16 | 0.10 | 0.23 | 0.19 | 2.2 | 1.9 | 2.1 | 4.9 | 1.5 | 7.2 | 5.2 | 4.5 |
| 19008+0726 | 6.0 | 5.8 | 6.5 | 0.72 | 0.64 | 0.35 | 0.75 | 0.71 | 7.7 | 6.0 | 7.6 | 4.8 | 1.5 | 7.2 | 4.9 | 4.6 |
| 19175–0807 | 6.2 | 6.0 | 6.7 | 0.80 | 0.71 | 0.39 | 0.82 | 0.78 | 10.2 | 7.9 | 10.1 | 5.4 | 1.7 | 7.9 | 5.4 | 5.1 |
| 19321+2757 | 4.5 | 4.4 | 4.9 | 1.0 | 0.87 | 0.50 | 1.0 | 0.98 | 12.9 | 9.9 | 12.8 | 6.3 | 2.0 | 9.3 | 6.3 | 6.0 |
| 19594+4047 | 11. | 11. | 12. | 1.1 | 0.97 | 0.51 | 1.1 | 1.0 | 11.2 | 8.6 | 11.0 | 3.2 | 1.0 | 4.7 | 3.2 | 3.0 |
| 20072+3116 | 7.3 | 7.0 | 7.9 | 0.90 | 0.82 | 0.43 | 0.95 | 0.89 | 7.7 | 6.0 | 7.6 | 3.8 | 1.2 | 5.7 | 3.9 | 3.7 |
| 20085–1425 | 2.1 | 1.7 | 2.5 | 0.16 | 0.12 | 0.086 | 0.20 | 0.15 | 1.7 | 1.5 | 1.6 | 5.9 | 1.9 | 8.7 | 6.4 | 5.3 |
| 20396+4757 | 3.9 | 3.5 | 4.6 | 0.20 | 0.17 | 0.10 | 0.23 | 0.19 | 2.1 | 1.8 | 2.1 | 4.5 | 1.4 | 6.7 | 4.8 | 4.2 |
| 20570+2714 | 6.2 | 6.1 | 6.8 | 1.1 | 0.93 | 0.52 | 1.1 | 1.0 | 14.3 | 11.0 | 14.2 | 5.4 | 1.7 | 8.0 | 5.4 | 5.1 |
| 21035+5136 | 5.9 | 5.1 | 7.1 | 0.18 | 0.15 | 0.093 | 0.21 | 0.17 | 2.3 | 2.0 | 2.2 | 3.7 | 1.2 | 5.5 | 3.9 | 3.3 |
| 21262+7000 | 2.7 | 2.3 | 3.1 | 0.15 | 0.12 | 0.077 | 0.18 | 0.14 | 1.8 | 1.6 | 1.7 | 6.1 | 1.9 | 9.0 | 6.6 | 5.6 |
| 21320+3850 | 4.3 | 3.9 | 5.0 | 0.25 | 0.21 | 0.13 | 0.28 | 0.24 | 3.0 | 2.5 | 2.9 | 4.7 | 1.5 | 6.9 | 4.9 | 4.3 |
| 22036+3315 | 0.48 | 0.42 | 0.57 | 0.14 | 0.083 | 0.084 | 0.17 | 0.13 | 2.0 | 1.8 | 2.0 | 20.0 | 6.3 | 29.7 | 21.5 | 18.4 |
| 23166+1655 | 16. | 15. | 19. | 2.0 | 1.9 | 0.97 | 2.1 | 2.0 | 11.4 | 8.8 | 11.0 | 1.6 | 0.5 | 2.3 | 1.6 | 1.4 |
| 23320+4316 | 9.4 | 8.8 | 11. | 0.54 | 0.48 | 0.26 | 0.58 | 0.52 | 5.1 | 4.1 | 5.0 | 2.7 | 0.9 | 4.1 | 2.8 | 2.5 |

(a) Model A is the standard model with $a=0.1 \mu\text{m}$, $\kappa_{60}=68 \text{ cm}^2 \text{ g}^{-1}$, $M_*=0.6 M_\odot$ and $v_0=1 \text{ km s}^{-1}$. Model B has $a=0.01 \mu\text{m}$, model C has $\kappa_{60}=150 \text{ cm}^2 \text{ g}^{-1}$, model D has $M_*=0.8 M_\odot$, and model E has $v_0=3 \text{ km s}^{-1}$. All other parameters are unchanged with respect to model A.

(b) Mass-loss rates are in units of $10^{-6} M_\odot \text{ yr}^{-1}$.

(c) Dust-to-gas ratios are in units of 0.01.

(d) Drift velocities in km s^{-1} .

7.3 Comparison with theoretical models

Two groups (Berlin and Vienna) calculate radiation-hydrodynamical models of the atmospheres and circumstellar shells of carbon-rich, long-period variables which include dust formation (see Höfner et al. 1996 for details and a comparison between the two groups). In this section we compare selected models with our derived parameters.

From the Vienna group we take the models of Höfner & Dorfi (1997). As pulsation period and luminosity are independent variables in these models, some combinations they calculate are not in agreement with the P – L relation we use in this paper. We therefore restrict ourselves to the following models (in their notation): P1, P2, P4, P5 (650 d, $10\,000 L_\odot$), R5, R5C (295 d, $5000 L_\odot$), R7, R7C20, R7C18 (390 d, $7000 L_\odot$). In all cases the stellar mass is $1 M_\odot$ in these models. The differences between the models of a given period and luminosity are the C/O ratio (for the 295- and 390-d models) and/or the effective temperature.

From the Berlin group we take the following models from Fleischer, Gauger & Sedlmayr (1992) and Arndt, Fleischer & Sedlmayr (1997), again only those with luminosities in accordance with our adopted P – L relation. In their notation these are: from Fleischer et al. models A (350 d, $4590 L_\odot$), B (322 d, $4310 L_\odot$), C (400 d, $6500 L_\odot$), E (650 d, $10\,000 L_\odot$), F (900 d, $15\,500 L_\odot$); from Arndt et al. models 2, 4, 9, 13–19, 22–24, 26–29 (all these 17 models with 650 d , $10\,000 L_\odot$), 34 (350 d, $5000 L_\odot$), 35 (400 d, $8500 L_\odot$), 36–37 (650 d, $10\,000 L_\odot$), 40 (400 d, $5000 L_\odot$), 41–43 (350 d, $5000 L_\odot$), 44 (350 d, $5500 L_\odot$), 47 (650 d, $10\,000 L_\odot$). Again the differences between models with the same period and luminosity are in stellar mass, effective temperature, C/O ratio and/or piston velocity amplitude. Additionally, we take the models specifically designed to fit IRC + 10216 (Winters, Fleischer & Sedlmayr 1997; 650 d, $24\,000 L_\odot$), which is a combination of period and luminosity that does not fit our P – L relation, and AFGL 3068 (Fleischer et al. 1997; 696 d, $13\,000 L_\odot$). Note that the models were not all calculated

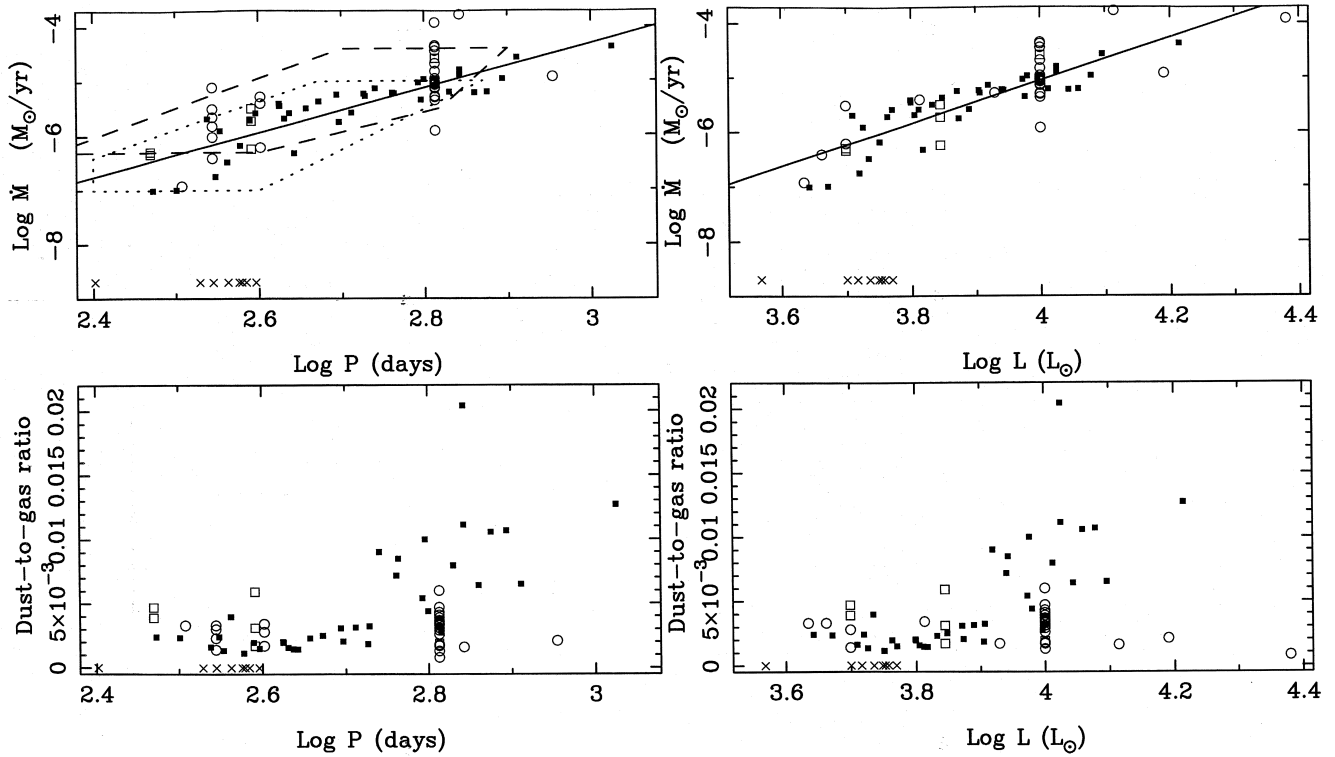


Figure 44. Mass-loss rate and dust-to-gas ratio, according to model A in Table 4, versus pulsation period and luminosity (filled squares). The crosses plotted at a mass-loss rate of $2 \times 10^{-9} M_{\odot} \text{ yr}^{-1}$ and $\Psi=0$ are stars without measured expansion velocity or for which no dust mass-loss rate could be derived. The solid lines are least-squares fits (see equations 9 and 10). The dashed and dotted polygons indicate regions occupied by different samples of oxygen-rich Miras (see text). The open squares and circles represent selected models from radiation-hydrodynamical calculations including dust formation from the Vienna and Berlin groups, respectively (see text).

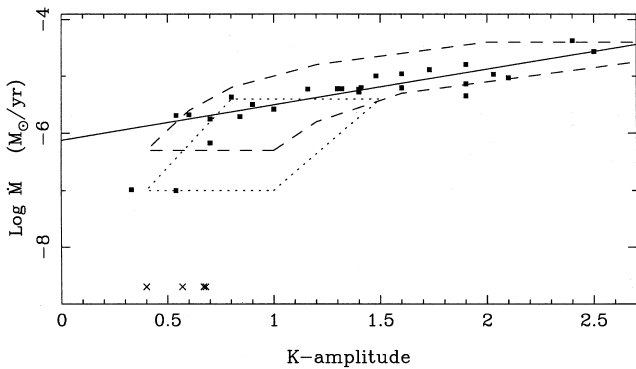


Figure 45. Mass-loss rate according to model A in Table 4, versus amplitude in the *K* band. The crosses plotted at a mass-loss rate of $2 \times 10^{-9} M_{\odot} \text{ yr}^{-1}$ are stars for which no dust mass-loss rate could be derived. The solid line is a least-squares fit (see equation 11). The dashed and dotted polygons represent the area where oxygen-rich stars in the Galactic Bulge and at high galactic latitude are located (see text).

with exactly the same physics (see Arndt et al. 1997 for details).

All of the models provide mass-loss rates, time-averaged dust-to-gas ratios and expansion velocities. The model results are plotted as the open squares (Vienna models) and open circles (Berlin models) in Figs 44 and 46.

In general, the mass-loss rates that these models predict are in good agreement with observed values derived in the present paper (Fig. 44), the exception being the models

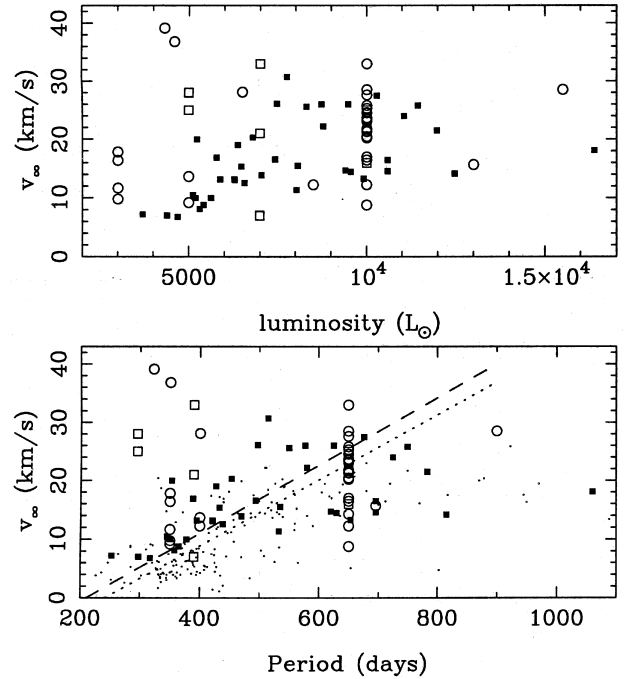


Figure 46. Observed expansion velocity plotted versus luminosity and pulsation period. The dashed and dotted lines are expressions in the literature for oxygen-rich stars (see text). The open squares and circles represent radiation-hydrodynamical model calculations (see text). The dots represent observed values of expansion velocities based on CO or OH observations for oxygen-rich Miras and OH/IR stars (see text).

specifically designed to fit IRC + 10216 (Winters et al. 1997) and AFGL 3068 (Fleischer et al. 1997). Apart from having a luminosity inconsistent with the $P-L$ relation, their proposed mass-loss rate of $1.2 \times 10^{-4} M_{\odot} \text{ yr}^{-1}$ for IRC + 10216 is larger than the upper limit of $4 \times 10^{-5} \text{ yr}^{-1}$ derived by Keady & Ridgway (1993) from the non-detection of the H_2 S(1) rotation line of $17.0 \mu\text{m}$. We find a mass-loss rate of $(1.1-1.3) \times 10^{-5} M_{\odot} \text{ yr}^{-1}$.

Regarding the dust-to-gas ratio there is good agreement for short periods and low luminosities, in particular if one considers that there may be systematic uncertainties due to the uncertainty in the absolute values of the dust opacity. For longer periods and higher luminosity there is a systematic difference in the sense that the theoretical models predict similar, and observations suggest higher, dust-to-gas ratios than at shorter periods.

Regarding the expansion velocities (Fig. 46), one notices that the theoretical models predict velocities for short-period/low-luminosity Miras which are too large compared with observations. This could be partly because the theoretical models neglect the drift velocity and thus predict the dust velocity, while the velocity which is observed is that of the gas. On the other hand, it is also clear that the C/O ratio predominantly determines the final velocity in the theoretical models. This is nicely demonstrated by the Vienna models at $7000 L_{\odot}$, or 390 d. As the C/O ratio goes up from 1.8 to 2.0 to 2.5, the expansion velocity goes up from 7 to 21 to 33 km s^{-1} , with all other parameters remaining the same. The observations therefore suggest a C/O ratio between 1.8 and 2.0 for stars of these luminosities. The two Berlin models at $5000 L_{\odot}$ (periods of 350 and 400 d) are in good agreement with the observations. They are calculated with C/O ratios of 1.50 and 1.60. At the shortest periods, the two Vienna models are calculated with C/O ratios of 2.30 and 2.50. The observations therefore imply C/O ratios smaller than about 2. At the lowest luminosities the four Berlin models are calculated with C/O ratios of 1.50 and 1.70. Again the observations imply C/O ratios smaller than this. This is consistent with the C/O ratios determined in 30 carbon-rich semiregular and irregular variables with little or no dust by Lambert et al. (1986), who find that the largest C/O ratio is 1.6, and 50 per cent of the stars in their sample have $C/O < 1.1$. An increase of the C/O ratio with luminosity is also consistent with an evolutionary picture in which stars with higher luminosity evolve from stars of higher initial mass; these have experienced more thermal pulses and thus dredged-up more carbon (see the scenario by Groenewegen et al. 1995).

The reason why the Berlin and Vienna groups calculate models with low luminosity only for large C/O ratios is that only under these conditions do their models predict outflows. This reveals a limitation of the current state of modelling. It could imply there is an additional outward-directed force besides radiation pressure on dust, possibly radiation pressure on molecules (Jørgensen & Johnson 1992), acoustic waves (Pijpers & Habing 1989), or Alfvén waves (Hartmann & MacGregor 1980). Alternatively, the flow may not be homogeneous, but clumpy, which could lead to localized dust formation. Clumpy structures are seen in the CO emission around the carbon stars with detached shells (e.g. Bergman, Carlström & Olofsson 1993; Olofsson et al. 1996).

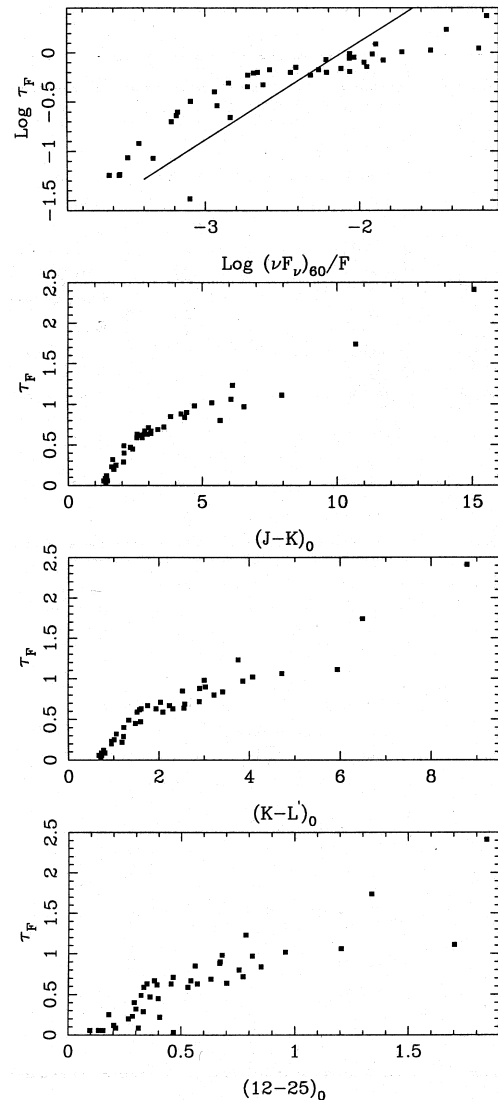


Figure 47. The flux-weighted optical depth versus $(\nu F_{\nu})_{60}/F$, $J-K$, $K-L'$ and $12-25$ synthetic colours (dereddened). The solid line in the top panel is the relation suggested by Ivezic & Elitzur (1995).

7.4 Colour versus optical depth

The procedure outlined in Section 6 to obtain the mass-loss rate and dust-to-gas ratio, under the assumption that mass-loss is driven by radiation pressure on dust, requires knowledge of the flux-weighted optical depth, τ_F . Unless one does the radiative transfer modelling, this quantity is unknown. Ivezic & Elitzur (1995) proposed a calibration of τ_F against $(\nu F_{\nu})_{60}/F$, not only for carbon-rich dust but also for silicate dust. In Fig. 47 τ_F is plotted against $(\nu F_{\nu})_{60}/F$, $J-K$, $K-L'$ and $12-25$ colour. The relation suggested by Ivezic & Elitzur (1995) is represented by the solid line. Our results differ significantly from their best fit. The reason is not immediately obvious. One reason for the discrepancy is that their line is intended to fit not only their results for a grain mixture of SiC and AMC (in a fixed ratio of 1:4), but also silicates + AME, olivine + silicates, and pure silicates and AMC. Their result for a mixture of SiC + AMC lies above the general fit and is also curved, similar to our result.

Nevertheless, the differences in Fig. 47 are larger than can be accounted for by this effect alone.

7.5 Colour versus period relations

In a recent paper, Lepine et al. (1995) discussed some relations between colours and pulsation period and/or luminosity for OH/IR stars. Here we attempt to extend this to a larger sample of oxygen-rich stars and make a comparison with the carbon star sample.

In order to circumvent the effect of variability, and the different photometric systems on which the infrared data were taken, we did not take the original observational data, but instead convolved our final model fits of the carbon stars

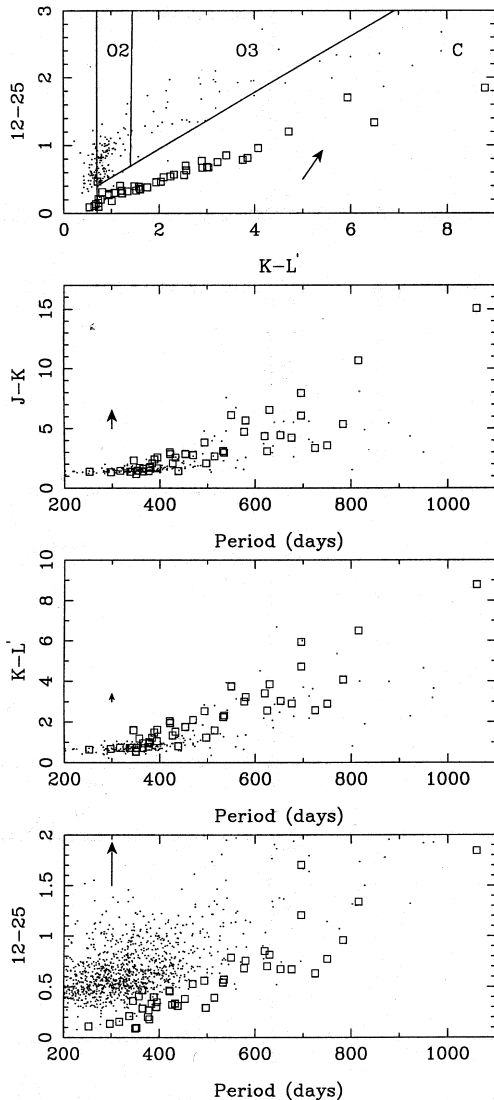


Figure 48. $[K-L']$ versus $[12-25]$ colour-colour diagram, and $[J-K]$, $[K-L']$ and $[12-25]$ colour versus pulsation period. The open squares represent the carbon Miras from the present sample, with dereddened synthetic colours. The dots represent observations of known oxygen-rich Miras and OH/IR stars (see text). The segments marked 'O2', 'O3' and 'C' indicate regions predominantly occupied by oxygen-rich and carbon stars, respectively (see Epchtein et al. 1987). The arrows mark the shift in colour when corrected for an A_V of 10 mag.

with the ESO $JHKL'M$ and *IRAS* photometric filter response curves, and applied the appropriate zero-points to obtain unreddened synthetic colours (see Groenewegen 1997b).

For the oxygen-rich stars this is not possible, and therefore the observed colours are shown without reddening correction. The sample selection of the oxygen-rich Miras and OH/IR stars is discussed in Appendix B. It is important to note that only photometry on the ESO system is plotted.

In Fig. 48 the synthetic colours of the carbon stars (open squares), and the observed colours for the oxygen-rich Miras and OH/IR stars (dots) are plotted against pulsation period (bottom three panels); these are all on the *IRAS* and ESO systems. There is a clear trend that redder colours are associated with longer periods. In fact, for periods longer than 450 d one may make a rough estimate of the period from the colours, if a given carbon star is thought to be a Mira variable but its period has not been determined. This could be particularly useful in statistical studies when large sets of infrared photometry are available of stars (e.g., the up-coming large-scale DENIS and 2MASS infrared surveys) for which no periods will generally be available.

The oxygen-rich and carbon stars behave similarly in the $J-K$ and $K-L'$ colour plots, but there is a significant offset in the $12-25$ colour. This is due to the strong silicate emission feature in oxygen-rich stars with optically thin shells. In the top panel of Fig. 48 the $12-25$ versus $K-L'$ colour-colour plot is shown (e.g. Epchtein et al. 1987). As shown in that paper, and confirmed here, oxygen-rich and carbon stars separate nicely in this colour-colour diagram. In practice, this means that in statistical studies one can use the $12-25$ versus $K-L'$ plots, or similar colour-colour plots, to distinguish carbon stars from oxygen-rich stars, and then use the colour versus period plots to infer the period. One could then use a $P-L$ relation to obtain the luminosity, and thus derive a distance estimate from the observed flux and a suitable bolometric correction (e.g. Groenewegen 1997b).

ACKNOWLEDGMENTS

The observations were obtained with the United Kingdom Infrared Telescope, operated by the Royal Observatory Edinburgh on behalf of the UK Science and Engineering Research Council, and with the Carlos Sanchez telescope, operated on the island of Tenerife in the Spanish Observatorio del Teide of the Instituto de Astrofísica de Canarias.

The research has made use of the SIMBAD data base, operated at CDS, Strasbourg, France. The 1994 observing trip of MATG to the Anglo-Australian Telescope and his subsequent stay at ADFA were made possible by financial support from the Franco-Australian fund for scientific collaboration. Suzanne Ramsay and Tom Geballe are thanked for taking the UKIRT CGS3 spectra. The United Kingdom Infrared Telescope is operated by the Joint Astronomy Research Council. Josef Wagenhuber is thanked for critically reading Appendix A. An anonymous referee made critical remarks which improved the presentation. Jacques Lepine and Roberto Ortiz are thanked for making their data base on OH/IR stars available in computer-readable form. This work is supported by the *Fonds zur Förderung der wissenschaftlichen Forschung* under project number S7308-

AST. We also thank Freddy Marang, Michael Feast and Brian Carter for making some of the infrared observations in Table 1.

REFERENCES

- Aitken D. A., Roche P. F., 1982, *MNRAS*, 200, 217
 Alknis A., 1980, *Invest. Sun Red Stars*, 11, 5
 Altenhoff W. J., Thum C., Wendker H. J., 1994, *A&A*, 281, 161
 Arndt T. U., Fleischer A. J., Sedlmayr E., 1997, *A&A*, in press
 Bagnulo S., Doyle J. G., Griffin I. P., 1995, *A&A*, 301, 501
 Barnes T. G., 1973, *ApJS*, 25, 369
 Bedijn P. J., 1987, *A&A*, 186, 136
 Bergeat J., Lunel M., 1980, *A&A*, 87, 139
 Bergeat J., Sibille F., Lunel M., Lefèvre J., 1976, *A&A*, 52, 227
 Bergman P., Carlström U., Olofsson H., 1993, *A&A*, 268, 685
 Burstein D., Heiles C., 1982, *AJ*, 87, 1165
 Cardelli J. A., Clayton G. C., Mathis J. S., 1989, *ApJ*, 345, 245
 Carter B. S., 1990, *MNRAS*, 242, 1
 Catchpole R. M., Robertson B. S. C., Lloyd Evans T. H. H., Feast M. W., Glass I. S., Carter B. S., 1979, *SAAO Circ.*, 1, 61
 Celis S. L., 1982, *AJ*, 87, 1791
 Chan S. J., Kwok S., 1990, *A&A*, 237, 354
 Chapman J. M., Habing H. J., Killeen N. E. B., 1995, in Stobie R. S., Whitelock P. A., eds, *ASP Conf. Ser. Vol. 83, Astrophysical Applications of Stellar Pulsation*. Astron. Soc. Pac., San Francisco, p. 113
 Cohen M., 1984, *MNRAS*, 206, 137
 Cohen M., Kuhl L. V., 1977, *PASP*, 89, 829
 Cohen M., Walker R. G., Witteborn F. C., 1992, *AJ*, 104, 2030
 Danchi W. C., Bester M., Degiacomi C. G., Greenhill L. J., Townes C. H., 1994, *AJ*, 107, 1469
 Dyck H. M., Lockwood G. W., Capps R. W., 1974, *ApJ*, 189, 89
 Eggen O. J., 1975, *ApJS*, 29, 77
 Engels D., Schultz G. V., Sherwood W. A., 1981, in Iben I., Renzini A., eds, *Physical Processes in Red Giants*. Reidel, Dordrecht, p. 401
 Engels D., Kreysa E., Schultz G. V., Sherwood W. A., 1983, *A&A*, 124, 123
 Epchtein N., Le Bertre B., Lépine J. R. D., Marques dos Santos P., Matsuura O. T., Picazzio E., 1987, *A&AS*, 71, 39
 Epchtein N., Le Bertre T., Lépine J. R. D., 1990, *A&A*, 227, 82
 Fleischer A. J., Gauger A., Sedlmayr E., 1992, *A&A*, 266, 321
 Fleischer A. J., Winters J.-M., Le Bertre T., Sedlmayr E., 1997, in Garzón F. et al., eds, *The Impact of Large Scale Near-infrared Surveys*. Kluwer, Dordrecht, p. 101
 Forrest W. J., Gillett F. C., Stein W. A., 1975, *ApJ*, 195, 423
 Fouqué P., Le Bertre T., Epchtein N., Guglielmo F., Kerschbaum F., 1992, *A&AS*, 93, 151
 Gail H.-P., Sedlmayr E., 1986, *A&A*, 161, 201
 Gaylard M. J., West M. E., 1995, in Stobie R. S., Whitelock P. A., eds, *ASP Conf. Ser. Vol. 83, Astrophysical Applications of Stellar Pulsation*. Astron. Soc. Pac., San Francisco, p. 113
 Gehrz R. D., Hackwell J. A., 1976, *ApJ*, 206, L161
 Gehrz R. D., Ney E. P., Grasdalen G. L., Hackwell J. A., Thronson H. A., 1984, *ApJ*, 281, 303
 Gillett F. C., Merrill K. M., Stein W. A., 1971, *ApJ*, 164, 83
 Gosnell T. R., Hudson H., Puetter R. C., 1979, *AJ*, 84, 538
 Grasdalen G. L., Gehrz R. D., Hackwell J. A., Castelaz M., Gullixson D., 1983, *ApJS*, 53, 413
 Griffin I. P., 1990, *MNRAS*, 247, 591
 Griffin I. P., 1993, *MNRAS*, 260, 831
 Groenewegen M. A. T., 1993, PhD thesis, Univ. Amsterdam, Chapter 5
 Groenewegen M. A. T., 1995a, *A&A*, 293, 463 (G95)
 Groenewegen M. A. T., 1995b, in Watt G. D., Williams P. M., eds, *Circumstellar Matter*. Kluwer, Dordrecht, p. 321
 Groenewegen M. A. T., 1995c, in Stobie R. S., Whitelock P. A., *ASP Conf. Ser. Vol. 83, Astrophysical Applications of Stellar Pulsation*. Astron. Soc. Pac., San Francisco, p. 141
 Groenewegen M. A. T., 1997a, *A&A*, 317, 503
 Groenewegen M. A. T., 1997b, in Garzón F. et al., eds, *The Impact of Large-scale Infrared Surveys*. Kluwer, Dordrecht, p. 165
 Groenewegen M. A. T., de Jong T., 1993, *A&AS*, 101, 267
 Groenewegen M. A. T., Whitelock P. A., 1996, *MNRAS*, 281, 1347
 Groenewegen M. A. T., de Jong T., van der Blik N. S., Slijkhuys S., Willems F. J., 1992, *A&A*, 253, 150
 Groenewegen M. A. T., de Jong T., Baas F., 1993, *A&AS*, 101, 513
 Groenewegen M. A. T., de Jong T., Geballe T. R., 1994, *A&A*, 287, 163
 Groenewegen M. A. T., van den Hoek L. B., de Jong T., 1995, *A&A*, 293, 381
 Groenewegen M. A. T., Baas F., de Jong T., Loup C., 1996a, *A&A*, 306, 241
 Groenewegen M. A. T., Baas F., Blommaert J. A. D. L., Josselin E., Tilanus R. P. J., 1996b, in Shaver P., ed., *Science with Large Millimetre Arrays*. ESO, p. 286
 Groenewegen M. A. T., van Loon J. TH., Whitelock P. A., Wood P. R., Zijlstra A. A., 1997, in *Proc. IAU Symp. 177, The Carbon Star Phenomenon*, in press
 Guglielmo F., Epchstein N., Le Bertre T., Fouglié P., Hron J., Kerschbaum F., Lépine J. R. D., 1993, *A&AS*, 99, 31
 Habing H. J., Tignon J., Tielens A. G. G. M., 1994, *A&A*, 286, 523
 Hackwell J. A., 1972, *A&A*, 21, 239
 Hartmann L., MacGregor K. B., 1980, *ApJ*, 242, 260
 Höfner S., Dorfi E. A., 1997, *A&A*, 319, 648
 Höfner S., Fleischer A. J., Gauger A., Feuchtinger M. U., Dorfi E. A., Winters J. M., Sedlmayr E., 1996, *A&A*, 314, 204
 Ivezić Z., Elitzur M., 1995, *ApJ*, 445, 415
 Ivezić Z., Elitzur M., 1996, *MNRAS*, 279, 1011
 Jiménez-Esteban F. M., García-Lario P., Manchado A., Engels D., 1997, in Garzón F. et al., eds, *The Impact of Large Scale Near-infrared Surveys*. Kluwer, Dordrecht, p. 103
 Joint *IRAS* Science Working Group, 1986, *IRAS Catalogs and Atlases, Low Resolution Spectrograph (LRS)*, *A&AS*, 65, 607
 Joint *IRAS* Science Working Group, 1986, *IRAS Catalogs and Atlases, Point Source Catalog (PSC)*, US Government Printing Office, Washington
 Joint *IRAS* Science Working Group, 1986, *IRAS Catalogs and Atlases, Explanatory Supplement*, US Government Printing Office, Washington
 Jones B., Merrill K. M., Puetter R. C., Willner S. P., 1978, *AJ*, 83, 1437
 Jones T. J., Bryja C. O., Gehrz R. D., Harrison T. C., Johnson J. I., Klebe D. I., Lawrence G., 1990, *ApJS*, 74, 785
 Jørgensen U. G., Johnson H. R., 1992, *A&A*, 265, 168
 Jørgensen U. G., Westerlund B. E., 1988, *A&AS*, 72, 193
 Jura M., 1984, *ApJ*, 286, 630
 Jura M., 1986, *ApJ*, 303, 327
 Jura M., 1987, *ApJ*, 313, 743
 Justtanont K., Tielens A. G. G. M., 1992, *ApJ*, 389, 400
 Justtanont K., Barlow M. J., Skinner C. J., Roche P. F., Aitken D. K., Smith C. H., 1996, *A&A*, 309, 612
 Keady J. J., Ridgway S. T., 1993, *ApJ*, 406, 199
 Kholopov P. N. et al., 1985, *General Catalog of Variable Stars (GCVS)*. Nauka, Moscow
 Krüger D., Sedlmayr E., 1997, *A&A*, 321, 227
 Kwan J., Hill F., 1977, *ApJ*, 215, 781
 Lambert D. L., Gustafsson B., Eriksson K., Hinkle K., 1986, *ApJS*, 62, 373
 Landolt U., 1968, *PASP*, 80, 680

- Landolt U., 1969a, *PASP*, 81, 134
 Landolt U., 1969b, *PASP*, 81, 381
 Landolt U., 1973, *PASP*, 85, 625
 Lázaro C., Hammersley P. L., Clegg R. E. S., Lynas-Gray A. E., Mountain C. M., Zdrozny A., Selby M. J., 1994, *MNRAS*, 269, 365
 Le Bertre T., 1987, *A&A*, 176, 107
 Le Bertre T., 1988a, *A&A*, 190, 79
 Le Bertre T., 1988b, *A&A*, 203, 85
 Le Bertre T., 1992, *A&AS*, 94, 377
 Le Bertre T., 1993, *A&AS*, 97, 729
 Lebofsky M. J., Rieke G. H., 1977, *AJ*, 82, 646
 Lebofsky M. J., Sargent D. G., Kleinmann S. G., Rieke G. H., 1978, *ApJ*, 219, 487
 Lépine J. R. D., Ortiz R., Epchtein N., 1995, *A&A*, 299, 453
 Lequeux J., Jourdain de Muizon M., 1990, *A&A*, 240, L19
 Le Sidaner P., Le Bertre T., 1993, *A&A*, 278, 167
 Le Squeren A. M., Sivagnanam P., Dennefeld M., David P., 1992, *A&A*, 254, 133
 Lockwood G. W., 1972, *ApJS*, 24, 375
 Lockwood G. W., 1974, *ApJ*, 192, 113
 Lockwood G. W., 1985, *ApJS*, 58, 167
 Lopez B., Perrier C., Mékarnia D., Lefèvre J., Gay J., 1993, *A&A*, 270, 462
 Lorenz-Martins S., 1996, *A&A*, 314, 209
 Lorenz-Martins S., Lefèvre J., 1993, *A&A*, 280, 567
 Lorenz-Martins S., Lefèvre J., 1994, *A&A*, 291, 831
 Loup C., Forveille T., Omont A., Paul J. F., 1993, *A&AS*, 99, 231
 Low F. J., Kurtz R. F., Vrba F. J., Rieke G. H., 1976, *ApJ*, 206, L153
 Martin P. G., Rogers C., 1987, *ApJ*, 322, 374
 Meadows P. J., Good A. R., Wolstencroft R. D., 1987, *MNRAS*, 225, 43p
 Merrill K. M., Stein W., 1976, *PASP*, 88, 294
 Mitchell R. M., Robinson G., 1980, *MNRAS*, 190, 669
 Munari U., Yudin B. F., Taranova O. G., Massone G., Marang F., Roberts G., Winkler H., Whitelock P. A., 1992, *A&AS*, 93, 383
 Neckel Th., Klare G., 1980, *A&AS*, 42, 251
 Netzer N., Elitzur M., 1993, *ApJ*, 410, 701
 Neugebauer G., Leighton R. B., 1969, *NASA SP-3047*
 Ney E. P., Merrill K. M., 1980, *AFGL-TR-80-0050*
 Nicolet B., 1978, *A&AS*, 34, 1
 Noguchi K., Kawara K., Kobayashi Y., Okuda M., Sato S., 1981, *PASJ*, 33, 373
 Nyman L.-A., Hall P. J., Le Bertre T., 1993a, *A&A*, 280, 551
 Nyman L.-A., Olofsson H., Johansson L. E. B., Booth R. S., Carlstrom U., Wolstencroft R., 1993b, *A&A*, 269, 377
 Olofsson H., Bergman P., Eriksson K., Gustafsson B., 1996, *A&A*, 311, 587
 Olson B. I., Richer H. B., 1975, *ApJ*, 200, 88
 Orofino V., Colangeli L., Bussoletti E., Blanco A., Fonti S., 1990, *A&A*, 231, 105
 Ortiz R., Maciel W. J., 1996, *A&A*, 313, 180
 Parenago P. P., 1940, *AZh*, 17, 3
 Pégourié B., 1988, *A&A*, 194, 335
 Pijpers F. P., Habing H. J., 1989, *A&A*, 215, 334
 Price S. D., Murdock T. L., 1983, *The Revised AFGL Infrared Sky Survey Catalog*, *AFGL-TR-83-0055*
 Richer H. B., 1971, *ApJ*, 167, 521
 Ridgway S. T., Carbon D. F., Hall D. N., 1978, *ApJ*, 225, 138
 Rouleau F., Martin P. G., 1991, *ApJ*, 377, 526
 Rowan-Robinson M., Harris S., 1983a, *MNRAS*, 202, 767
 Rowan-Robinson M., Harris S., 1983b, *MNRAS*, 202, 797
 Rowan-Robinson M., Lock T. D., Walker D. W., Harris S., 1986, *MNRAS*, 222, 273
 Sahai R., Liechti S., 1995, *A&A*, 293, 198
 Salpeter E. E., 1974, *ApJ*, 193, 585
 Salpeter E. E., 1977, *ARA&A*, 15, 267
 Schutte W. A., Tielens A. G. G. M., 1989, *ApJ*, 343, 369
 Simon T., 1976, *AJ*, 81, 764
 Sivagnanam P., Braz M. A., Le Squeren A. M., Tran Minh F., 1994, *A&A*, 233, 112
 Sopka R. J. et al., 1985, *ApJ*, 294, 242
 Strecker D. W., Ney E. P., 1974, *AJ*, 79, 797
 te Lintel Hekkert P., Caswell J. L., Habing H. J., Hayes R. F., Norris R. P., 1990, *A&AS*, 90, 327
 te Lintel Hekkert P., Versteeg-Hensel H. A., Habing H. J., Wiertz M., 1989, *A&AS*, 78, 399
 Vassiliadis E., Wood P. R., 1993, *ApJ*, 413, 641
 Walker A. R., 1979, *SAAO Circ.*, 1, 112
 Whitelock P. A., 1990, in Cacciari C., Clementini G., eds, *ASP Conf. Ser. Vol. 11, Confrontation between Stellar Pulsation and Evolution*. *Astron. Soc. Pac.*, San Francisco, p. 365
 Whitelock P. A., Menzies J., Feast M. W., Marang F., Carter B., Roberts G., Catchpole R., Chapman J., 1994, *MNRAS*, 267, 711
 Whitelock P. A., Feast M. W., Marang F., Overbeek M. D., *MNRAS*, 1997, 288, 512
 Winters J. M., 1994, PhD thesis, Technische Universität Berlin
 Winters J. M., Fleischer A. J., Gauger A., Sedlmayr E., 1994, *A&A*, 290, 623
 Winters J.-M., Fleischer A. J., Sedlmayr E., 1997, in Paresce F., ed., *Science with the VLT interferometer*. Springer-Verlag, p. 403
 Wood P. R., 1990, in Mennessier M. D., Omont A., eds, *From Miras to Planetary Nebulae*. Editions Frontières, Gif-sur-Yvette, p. 67
 Woolf T. G., 1973, *ApJ*, 185, 229
 Zuckerman B., Dyck H. M., 1986, *ApJ*, 304, 394

APPENDIX A: A SELF-CONSISTENT DETERMINATION OF MASS-LOSS RATE AND EXPANSION VELOCITY?

There has been much debate on the meaning and applicability of the formula $\dot{M} = L/(cv_\infty)$. It has been argued that the true mass-loss rate must be lower than that derived from this equation (see, e.g., Jura 1984, Zuckerman & Dyck 1986 and Vassiliadis & Wood 1993). However, this is not the case (see Salpeter 1974 and Gail & Sedlmayr 1986).

Recently, Netzer & Elitzur (1993) and Ivezić & Elitzur (1995) showed that $\dot{M}[v(r) - v(r_{\text{inner}})] = \tau_F(r)L/c$, or $\dot{M}v_\infty = \tau_F(L/c)(1 - 1/\Gamma)$ (when gravity is included) are the correct formula, where Γ is the ratio of the radiative to gravitational force.

In these equations, the gas velocity is usually assumed to be known, e.g., taken from CO and/or OH observations. In other words, if Γ were known, and the flux-weighted optical depth derived from radiative transfer modelling, the mass-loss rate could be calculated.

As shown below, the value of Γ can be written down exactly, but is then in a form not suitable for practical application. A second point discussed below is that the same basic force equation can be solved to give the velocity structure. Since the terminal velocity of the wind is known from observations, this in principle gives a constraint on the radial dependence of the opacity in the wind.

The momentum equation for the gas, assuming that the outward force is radiation pressure, is

$$\rho v \frac{dv}{dr} = \frac{\kappa_F L}{4\pi r^2 c} - \frac{\rho G M_*}{r^2}, \quad (\text{A1})$$

where κ_F is the flux-averaged absorption coefficient at radius r . With mass conservation, this can be rewritten as

$$\dot{M} \frac{dv}{dr} = \frac{L}{c} \kappa_F - 4\pi GM_* \rho. \quad (\text{A2})$$

The only quantities that depend on r are v , κ_F and ρ ; all the others are constant. Integration gives

$$\dot{M}(v - v_0) = \frac{L}{c} \tau_F(r) - 4\pi GM_* \int_{r_0}^r \rho dr, \quad (\text{A3})$$

where r_0 and v_0 are the radius and velocity at the inner boundary and $\tau_F(r) = \int_{r_0}^r \kappa_F(r) dr$. Taking the $r \rightarrow \infty$ limit gives

$$\dot{M}(v_\infty - v_0) = \tau_F \frac{L}{c} \left[1 - \frac{1}{\Gamma^{(1)}} \right], \quad (\text{A4})$$

where $\tau_F = \tau_F(r \rightarrow \infty)$ and

$$\Gamma^{(1)} = \frac{L}{4\pi c GM_*} \frac{\int_{r_0}^\infty \kappa_F(r) dr}{\int_{r_0}^\infty \rho dr}. \quad (\text{A5})$$

This relation is exact.

Alternatively, equation (A1) can be rewritten as

$$v \frac{dv}{dr} = \frac{\chi_F L}{4\pi r^2 c} - \frac{GM_*}{r^2}, \quad (\text{A6})$$

where χ_F is the flux-average of $\chi_v = \kappa_v / \rho$, the absorption coefficient per unit mass. This gives

$$\frac{dv^2}{dr} = \frac{2GM_*}{r^2} [\Gamma^{(2)} - 1], \quad (\text{A7})$$

where

$$\Gamma^{(2)} = \frac{L}{4\pi c GM_*} \frac{\kappa_F(r)}{\rho(r)}. \quad (\text{A8})$$

$\Gamma^{(2)}$ can be rewritten using the definition of $\kappa_F = \pi a^2 Q_F n_d(r)$ and the continuity equation for the dust [$\dot{M}_d = 4\pi r^2 n_d(r) m_d v_d(r)$] and the gas [$\dot{M} = 4\pi r^2 \rho v(r)$] as

$$\Gamma = \frac{3 Q_F L \Psi v(r)}{16\pi a \rho_d c GM_* v_d(r)}, \quad (\text{A9})$$

where $n_d(r)$ is the dust particle number density, and $m_d = \frac{4}{3} \pi a^3 \rho_d$, the mass of a single dust particle.

Equation (A7) can be solved to give

$$v^2 - v_0^2 = \frac{L}{2\pi c} \int_{r_0}^r \frac{\chi_F dr}{r^2} - 2GM_* \left(\frac{1}{r_0} - \frac{1}{r} \right), \quad (\text{A10})$$

again an exact result within the model assumptions.

From equation (A10), the velocity at infinity can be written as

$$v_\infty^2 - v_0^2 = \frac{2GM_*}{r_0} [\Gamma^{(3)} - 1], \quad (\text{A11})$$

where

$$\Gamma^{(3)} = \frac{L}{4\pi c GM_*} \int_{r_0}^\infty r_0 \frac{\chi_F(r)}{r^2} dr. \quad (\text{A12})$$

Equations (A1) and (A6) are completely equivalent, and so are their solutions (A3) and (A10). In other words, back-substituting the velocity solution $v(r)$ from equation (A10) in equation (A3) should give an identity.

Direct application of equation (A4) to derive the mass-loss rate is hindered by the fact that Γ depends on integral quantities that are unknown. Below an approximation is introduced to circumvent this. It is explicitly verified that with this approximation the self-consistency between equations (A4) and (A11) is not violated.

Assuming that $\Gamma^{(2)}$ (or simply Γ hereafter) is independent of radial distance, equation (A7) can be integrated, using $v = v_0$ at $r = r_0$ as a boundary condition (see, e.g., Habing et al. 1994):

$$v^2(r) = v_0^2 + 2GM_* (\Gamma - 1) \left(\frac{1}{r_0} - \frac{1}{r} \right), \quad (\text{A13})$$

from which it follows that the terminal gas velocity is

$$v_{\text{theory}} = \sqrt{v_0^2 + \frac{2GM_*}{r_0} (\Gamma - 1)}. \quad (\text{A14})$$

Next the dust velocity law needs to be derived. Its radial dependence should be very similar to equation (A13) to fulfil the requirement that Γ is independent of radius, as we will replace $Q_F(r)$ by $Q_F(\infty)$. However, we need to manipulate equation (A13) to arrive at an equation that can be integrated analytically. As v_0 should be important only close to r_0 , equation (A13) is written in the form

$$v_d^2(r) = v_0^2 \left(\frac{r_0}{r} \right) + (v_{\text{theory}}^2 - v_0^2) \left(1 - \frac{r_0}{r} \right), \quad (\text{A15})$$

where the ‘fudge-factor’ (r_0/r) gives the exact formula for $r = r_0$. Rearranging terms, the shape of the dust velocity law can be written as (also see Habing, Tignon & Tielens 1994):

$$v_d(r) = v_d(\infty) \sqrt{\frac{x - y_0}{x}}, \quad (\text{A16})$$

with $x = r/r_0$, and y_0 defined as

$$y_0 = 1 - \frac{v_0^2}{v_\infty^2 - v_0^2}. \quad (\text{A17})$$

The continuity equation of the dust specifies that

$$\dot{M}_d = 4\pi r^2 v_d(r) n_d(r) m_d. \quad (\text{A18})$$

Combined with the definition of the optical depth

$$\tau_\lambda = \int_{r_0}^\infty \pi a^2 Q_\lambda n_d(r) dr, \quad (\text{A19})$$

it follows that

$$\tau_\lambda = \frac{(3Q_\lambda/4a\rho_d)\dot{M}_d}{4\pi v_d(\infty)r_0} \int_1^\infty \frac{1}{\sqrt{(x-y_0)/x}} \frac{1}{x^2} dx. \quad (\text{A20})$$

The integral can be evaluated analytically, and the result is $Y \equiv (2/y_0)(1 - \sqrt{1-y_0})$. Now we are ready to proceed.

By construction the radial dependence of the gas and dust velocity are essentially equal, and $v(r)/v_d(r)$ is replaced by $v(\infty)/v_d(\infty)$. Using the definition of the dust-to-gas ratio ($\Psi = \dot{M}_d/\dot{M}$), Γ can be written as

$$\Gamma = \frac{(3Q_F(\infty)/4a\rho_d)Lv_\infty \dot{M}_d}{4\pi cGM_*v_d(\infty) \dot{M}}. \quad (\text{A21})$$

For the dust mass-loss rate, we invert equation (A19) and substitute it in equation (A21):

$$\Gamma = \frac{Q_F \tau_\lambda L r_0 v_\infty}{Q_\lambda c G M_* Y \dot{M}} \frac{1}{M}. \quad (\text{A22})$$

For the mass-loss rate, we now substitute equation (A4), with $\Gamma^{(1)}$ replaced by Γ :

$$\dot{M} = \tau_F \frac{L/c}{v_\infty - v_0} \left(1 - \frac{1}{\Gamma}\right). \quad (\text{A23})$$

This results in:

$$\Gamma - 1 = \left(\frac{Q_F \tau_\lambda}{Q_\lambda \tau_F} \right) \frac{r_0 v_\infty (v_\infty - v_0)}{GM_* Y}. \quad (\text{A24})$$

The first term between parentheses is identical to unity, because $\tau_\lambda \sim Q_\lambda$, and similarly for the flux-weighted quantity. Substituting the expression for Γ into equation (A14) gives

$$v_{\text{theory}} = \sqrt{v_0^2 + v_\infty (v_\infty - v_0) y_0 / (1 - \sqrt{1-y_0})}. \quad (\text{A25})$$

One can make an expansion in (v_0/v_∞) and show that

$$v_{\text{theory}} = v_\infty \sqrt{1 + \frac{1}{2}(v_0/v_\infty)^3 + Q[(v_0/v_\infty)^4]}. \quad (\text{A26})$$

This shows that, for the given approximations for Γ , equations (A14) and (A24) are self-consistent to a very high degree.

As the model fits were made taking a constant velocity while the approach to calculate the mass-loss rate requires a certain dust velocity law, a correction to the originally derived dust mass-loss rates must be made. As the fits to the SEDs depend exclusively on the optical depth, this implies that the dust mass-loss rates listed in Table 3 have to be divided by Y , following equation (A20).

APPENDIX B: SELECTION OF A SAMPLE OF OXYGEN-RICH MIRAS AND OH/IR STARS

To compare some observational properties of carbon stars and oxygen-rich stars, a sample of oxygen-rich Miras and

OH/IR stars is constructed. The primary interest is in period, near-infrared photometry on the ESO system, and expansion velocity.

For practical purposes the data gathering was done in two steps, namely that regarding optical Miras and that concerning OH/IR stars. One of us (FK) selected from the fourth edition of the GCVS all oxygen-rich confirmed Miras with confirmed periods with an *IRAS* FQUAL = 3 detection at 12 and 25 μm . This sample amounts to 1138 stars. For 133 of these *JHKL'M* photometry is available on the ESO system. The photometry is taken from a data base compiled by one of the authors (FK). For 32 stars the expansion velocity based on CO data is available from Loup et al. (1993), and for another 16 from Groenewegen et al. (1996b). To have a larger sample of expansion velocities, OH data were considered. This search was helped by the information provided by Drs J. Lepine and R. Ortiz, who provided their data base on OH/IR stars (private communication; Lepine et al. 1995; Ortiz & Maciel 1996). This provided expansion velocities for 83 oxygen-rich Miras, 64 of which have no CO velocity. When both are available, the CO velocity is preferred. The OH velocity is multiplied by a factor of 1.12, for reasons discussed below.

Regarding the OH/IR stars, the first step was to search the literature for pulsation periods. This search was also helped by the information provided by Drs Lepine and Ortiz, but done independently. Periods were taken from Engels, Schultz & Sherwood (1981), Engels et al. (1983), Lockwood (1985), Jones et al. (1990), Le Bertre (1993), Whitelock et al. (1994), Chapman, Habing & Killeen (1995), Gaylard & West (1995), Jiminez-Esteban et al. (1997) and Joyce et al. (1997, in preparation). Searches specifically aimed at finding OH/IR stars in the Galactic Bulge are excluded, as the associated photometry may be more susceptible to interstellar extinction than the presumably local sample selected now.

Stars already in the GCVS sample were excluded. 92 stars remain. Near-infrared photometry on the ESO system was compiled for 70 stars (Engels et al. 1981, 1983; Fouqué et al. 1992; Guglielmo et al. 1993; Le Bertre 1993; Nyman, Hall & Le Bertre 1993a), as well as CO velocities for 35 stars (Loup et al. 1993) and OH velocities for 67 stars (te Lintel Hekkert et al. 1989, 1990; Le Squeren et al. 1992; Sivagnanam et al. 1994), when available. Note that in some cases the OH profiles show only one peak, in which case no OH expansion velocity is available.

It is common to derive the CO expansion velocities from half the width at zero intensity, while it is common to derive the OH expansion velocity as half the width between the two peaks. The latter underestimates the true terminal velocity. From 22 stars with both CO and OH velocity, the geometric mean value of $v(\text{CO})/v(\text{OH})$ is 1.12. The CO velocity is preferred over the OH velocity. When no CO velocity is available, the OH velocity multiplied by 1.12 is used.